IMAGE PROCESSING TECHNIQUES FOR SPACE SITUATIONAL AWARENESS

YORK UNIVERSITY

MICHAEL IAN STEWART

A THESIS SUBMITTED TO THE FACULTY OF GRADUATE STUDIES
IN PARTIAL FULFILMENT OF THE REQUIREMENTS
FOR THE DEGREE OF
MASTER OF SCIENCE

GRADUATE PROGRAM IN EARTH AND SPACE SCIENCE
YORK UNIVERSITY
TORONTO, ONTARIO

29 APRIL 2024

Abstract

With a renewed interest in space, it is paramount to understand the space environment; an act commonly referred to as Space Situational Awareness (SSA). Tracking and performing measurements on nearby orbiting objects; known as RSOs helps us better understand SSA. Image processing is a significant step in improving SSA capabilities, aiding in space object detection, tracking, and characterization. This thesis addresses gaps in RSO image processing, with a focus placed on developing specialized pipelines for the production of photometric measurements of Geosynchronous Equatorial Orbit (GEO) RSOs and the James Webb Space Telescope (JWST). Despite challenges like the unique Earth-Sun L2 Orbit of JWST and high noise issues, this study successfully produced calibrated photometric light curves of three targeted RSOs, advancing our understanding of photometric SSA methodologies.

Acknowledgements

I would like to spend this time to thank all the people in my life who helped make this thesis possible. Foremost, I am eternally grateful for my core family who encouraged me along this path and whose decisions have set me up for success. I want to give praise to my supervisor, Regina Lee, who gave me the opportunity to join her lab, was flexible in dealing with COVID-19, was understanding of personal issues and assisted me in landing an internship with DRDC. I also wish to thank the folks at DRDC who were patient with teaching me industry standards and providing me with the resources required for my research. Furthermore, I am thankful for my extended family who provided me with a home away from home while I attended my internship in Ottawa. I am grateful for all the friends that I have met along my journey and appreciate them for their love and support . Lastly, I would like to recognize my partner for her love and lattes.

Table of Contents

List of Tables

List of Figures

Acronyms

ADU Analog-to-Digital Units.

AMOS Advanced Maui Optical and Space Surveillance Technologies.

APASS American Association of Variable Star Observers Photometric All-Sky Survey.

API Application Programming Interface.

CASI Canadian Aeronautics and Space Institute.

CASJ Canadian Aeronautical and Space Journal.

COE Classic Orbital Elements.

DRDC Defence Research and Development Canada.

DSS Digitized Sky Survey.

ECI Earth Centered Inertial.

EOP Earth Orientation Parameter.

FITS Flexible Image Transport System.

FOV Field of View.

GBO Ground Based Observatory.

GCFR Geocentric Celestial Reference Frame.

GEO Geosynchronous Equatorial Orbit.

GMST Greenwich Mean Sidereal Time.

HEOSS High Earth Orbit Space Surveillance.

IRAF Image Reduction and Analysis Facility.

JPL Jet Propulsion Laboratory.

JWST James Webb Space Telescope.

LEO Low Earth Orbit.

LST Local Sidereal Time.

NEO Near-Earth Object.

NEOs Near-Earth Objects.

NEOSSat Near-Earth Object Surveillance Satellite.

NORAD North American Aerospace Defense Command.

PSF Point Spread Function.

RAAN Right Ascension of the Ascending Node.

RSO Resident Space Object.

SDSS The Sloan Digital Sky Survey.

SEP Source Extraction and Photometry Package.

SEZ Topocentric-Horizon Coordinate System.

SGP Simplified General Perturbations.

SIP Simple Imaging Polynomial.

SNR Signal-to-noise ratio.

SSA Space Situational Awareness.

SSM Sidereal Stare Mode.

TEME True Equator, Mean Equinox.

TLE Two Line Element.

TRM Track Rate Mode.

UCAC4 The Fourth US Naval Observatory CCD Astrograph Catalog.

UTC Coordinated Universal Time.

WCS World Coordinate System.

WGS World Geodetic System.

Chapter 1

Introduction

1.1 Space Situational Awareness (SSA)

Space Situational Awareness (SSA), the act of tracking and monitoring space fairing objects close to Earth, known as Resident Space Object (RSO)s, stands at the forefront of modern space operations with the evolving space environment. As projections for 2030 estimate a two to ten times increase in RSO population, the restricted operating space causes considerable complications for object avoidance. [28]. SSA attempts to continuously catalogue new and existing RSOs through orbit determination techniques and other characteristics that can be extracted through photometry, such as tumble rate, and bus type.

1.2 Image Processing and Photometry

Photometry: the measuring of light from celestial bodies is of fundamental importance to characterizing RSOs. It provides scientists and researchers with direct measurements of the energy reflected at a variety of wavelengths and thus sets constraints for spacecraft modelling. Photometry, no matter the object, requires a processing pipeline, typically starting with data reduction, and ending with the extraction of a calibrated light curve. The data reduction segment of the pipeline aims to scrub away excess signal generated by the instrumentation itself. In optical astronomical practices, this includes the use of bias frames, dark frames and flat frames to compensate for different characteristics of the sensor. After data reduction, the light can then be measured using different methods such as Point Spread Function (PSF) photometry and aperture photometry to produce an instrumental magnitude. The amount of light received by a sensor differs drastically depending on many aspects including the filter used, airmass, and intrinsic sensor characteristics. For this reason, the instrumental magnitude must be calibrated into a standard system such as Bessel [9] or SLOAN [46] for comparison with data at different airmasses or taken by different sensors. This calibration is done through either differential photometry or absolute photometry depending on the data's characteristics. The resultant apparent magnitudes produced form these calibrations are plotted against time, forming a calibrated light curve.

1.3 Motivation

Performing photometry on RSOs assists in characterizing spacecraft including feature analysis [49], tumble rates [10], solar panel degradation [6], and RSO correlation [17]. Although processing pipelines exist for distant celestial objects, there is limited research on Near-Earth Objects (NEOs), specifically RSOs. Creating the tools for image processing of RSOs with open-source software contributes to the ongoing data collection process for more advanced SSA. This thesis covers acquisition of data, and the novel image-processing techniques used for performing photometry on RSOs.

1.4 Research Objectives

The research goals aimed at leveraging open-source software to generate standardized tools for different types of SSA photometry, including absolute photometry, differential photometry and space-based photometry. The objectives for this research were laid out below:

1. Investigate photometry pipeline.

   Review literature relevant to measuring celestial objects and devise a rough outline on how to apply these methods to RSOs.

2. Choose RSOs.

   RSOs are to be chosen depending on their research interests and requirements. The chosen RSOs are described in section 3.1.

3. Observe chosen RSOs.

   Conduct observations of chosen RSOs with the sensors available. The RSO must be easily discernible, having a SNR of at least 3 and located in a field that isn't too saturated with stars.

4. Develop photometric image processing pipeline. This is developed using methods described in Section 2.4.

   Apply the concepts investigated in the first objective to develop case-specific photometric pipelines. This objective is broken down further for the photometry steps and cases:

   (a) Develop image reduction tools based on observations.

   (b) Development of photometry pipelines:

      i. Absolute Photometry.

      ii. Differential Photometry.

iii. Space-based Photometry.

5. Implement pipeline steps.

   Create software that processes the images to extract their calibrated light sources.

1.5 Methodology

To fulfill the research goals, three unique datasets were collected of targeted RSOs. The first dataset, captured images of IntelSat 10-02 data from a contracted ground station in St.Johns Newfoundland, along with Landolt Star Fields for the application of absolution photometry. Secondly, images of Anik F1 were captured using Defence Research and Development Canada (DRDC)'s mobile Ground Based Observatory (GBO) for the primary purpose of performing differential photometry. Lastly, images with the space-based sensor Near-Earth Object Surveillance Satellite (NEOSSat) captured images of James Webb Space Telescope (JWST) as it approached the Earth and became visible. Each dataset possessed its own set of challenges from identifying multiple satellites in the same image to approximating the locations of non-keplarian orbits.

1.6 Research Tools

Photometric image processing was completed using the open-source *AstroPy* community Python library [2] [3] [4]. Specific packages of importance include *ccdproc* [13] used for data reduction, *astroplan* [32] for planning observations, *astroquery* [18] for querying catalogue values of stars and connecting to astrometry.net for plate solving [27], and *PhotUtils* [11] for image processing. Other notable Application Programming Interface (API)s and packages available outside the AstroPy library include: Brandon Rhode's *SkyField* [36] for satellite propagation leveraging SGP4 [29] and Jet Propulsion Laboratory (JPL) Horizons[19] API for estimating non-keplarian RSO positions.

1.7 Thesis Outline

This thesis is divided into 5 chapters; chapter 1 introduces the reader to SSA, observing RSOs and the importance of photometry. Chapter 2 provides the background material required for observing RSOs, image processing and performing photometry on RSOs. Chapter 3 illustrates how the concepts discussed in chapter 2 are applied. It covers choosing RSOs, predicting their locations, tracking them and processing the images. Chapter 4, covers the results that are produced from applying different photometry methods. Chapter 4.5 and 5 conclude the thesis with a discussion of the produced results and concluding statements.

1. Introduction (Chapter 1)

2. Background (Chapter 2)

3. Methods (Chapter 3)

4. Results (Chapter 4)

5. Conclusion (Chapter 5)

Chapter 2

Background

Performing photometry of RSOs requires a theoretical background of astrometric techniques and orbital dynamics. The following section aims to provide readers with an understanding of the underlying concepts and ends with examples in literature of similar topics.

2.1 Astronomical Equations

Jean Meeus' *Astronomical Algorithms*[31] provides background knowledge on the mathematics required to perform astronomical measurements. These are also presented in Valldo's *Fundamentals of Astrodynamics and Applications* [15] and *Orbital Mechanics for Engineering Students, Second Edition* [14]. The following subsections describe the main equations used in this thesis.

2.1.1 World Geodetic System

Earth can be estimated by an oblate reference ellipsoid standard; one of the most commonly used is the World Geodetic System (WGS). The WGS system allows a description of the location of an object with latitude, longitude and altitude (See Section 2.1.1). The WGS has multiple versions, with the latest 2014 revision WGS84 commonly used in this paper. This version's parameters include a semi-major axis (**a**) of 6,378,137m and a semi-minor axis (**b**) of 6,356,752m. Likewise, the values for the WGS 72 Ellipsoid are **a**: 6378135m and **b**: 6356750.520m. The WGS72 reference ellipsoid is also commonly used in the Simplified General Perturbations (SGP)4 Propagator used to propagate satellites from TLE (Section 2.2.2).[5]

Latitude and Longitude

Latitude and Longitude are geographical coordinates using a WGS model to pinpoint a specific location on Earth's surface. Latitude measures the north-south position from the equator, while longitude indicates the east-west position from the prime meridian, providing a global system for navigation and mapping. Geodetic Latitude (simply Latitude) is represented as **L** while λ_E represents the Geodetic Longitude. When converting between the Topocentric-Horizon Coordinate System (Section2.2.3) and Geocentric Systems, a measure of the local geodetic latitude and longitude must be considered (Section 2.3). While geocentric latitude is defined as the angle between equatorial plane to a point on the Earth's surface measured from the Earth's center, geodetic latitude takes into account Earth's irregular shape given a WGS model. Geodetic latitude is thus measured offset from the center of the Earth along the equatorial plane. [44]

2.1.2 Time

Proper, accurate accounts of time must be recorded along with the data acquired to ensure data integrity. The primary form of universal time distribution used today is Coordinated Universal Time (UTC), with offsets applied for timezones and daylight savings time.

Sidereal Time

Approximately 24 hours represents the time it takes for the sun to cross the celestial meridian; commonly known as a day. In contrast, a sidereal day, measures the time it takes for a reference star to cross the same meridian. Due to the Earth's orbit around the Sun, one mean solar day completes 1/365 of this orbit, making it a few minutes longer than a sidereal day when measured in solar time.

UT1 and UTC

Precise calculations of satellite orbits require the use of **UT1** Time, a time standard corrected for the effects of perturbations of Earth. As the Coordinated Universal Time (UTC) is the most common method for time measurement and distribution, it must be compensated for by Equation 2.1.

$$UTC = UT1 - \Delta UT1 \tag{2.1}$$

$\Delta UT1$ continuously changes and is predicted daily by the Earth Orientation Parameter (EOP) Product Center. The EOP website must be queried at an observation date to find the appropriate UT compensation value. [33]

Local Sidereal Time

The Local Sidereal Time (LST) is important information required for converting between a Topocentric-Horizon Coordinate System (Section 2.2.3) to an ECI system (Sections 2.2.3 2.3.3). Local Sidereal Time (LST) is represented in this paper by θ_{LST}

.

To calculate LST Equations 2.2 to 2.7 are used. [15]

$$\theta_{LST} = \theta_{GMST} + \lambda_e \tag{2.2}$$

$$\theta_{GMST} = 67310.54841^s + (876600^h + 8640184.812866^s)*$$

$$T_{UT1} + 0.093104T_{UT1}^2 - 6.2(*10^{-6})T_{UT1}^3 \tag{2.3}$$

$$T_{UT1} = \frac{JD_{UT1} - 2451545}{36525} \tag{2.4}$$

$$JD_{UT1} = INT(365.25(yr + 4716))$$

$$+INT(30.6001(mo + 1)) + d + B - 1524.5 + C \tag{2.5}$$

$$B_{UT1} = 2 - INT(\frac{yr}{100}) + INT(\frac{INT\frac{yr}{100}}{4}) \tag{2.6}$$

$$C_{UT1} = \frac{\frac{(\frac{s}{60*}) + min}{60} + h}{24} \tag{2.7}$$

Where:

- yr: year measured in UT1
- s: second measured in UT1
- min : minutes measured in UT1
- INT : real number truncation
- JD: Julian Date
- $GMST$: Greenwich Mean Sidereal Time (GMST) (degrees)

Note that in the conversion of Gregorian Dates to Julian Dates the months of January and February are treated as the 13 and 14. If the month is equal to 1 or 2, then the year is reduced by 1 and $mo = mo + 12$.

2.2 Describing RSOs

In the realm of astrodynamics, there are several books that are commonly used to establish an understanding of the subject. These include *Fundamentals of Astrodynamics* by Bate and Mueller [5], and *Fundamentals of Astrodynamics and Applications* by Vallado [44]. The following sections describe how to model spacecraft in different frames and transform the models into localized frames for accurate observations.

Regardless of the coordinate system in which an RSO is perceived, six parameters are required to describe the object at a given epoch. As discussed below, RSOs can be in the form of state vectors or element sets such as TLE sets or COEs as described in the following sections. [5][25]

2.2.1 State Vectors

Orbital state vectors are vectors describing an object's positions and velocity at a given epoch time represented in a reference frame. They can be expressed in both spherical coordinates and more commonly Cartesian coordinates. An example of an RSO state vector in the ECI frame is seen in Equation 2.8.

$$\vec{x}(t) = \begin{bmatrix} x_{\mathbf{I}}(t) \\ x_{\mathbf{J}}(t) \\ x_{\mathbf{K}}(t) \\ v_{\mathbf{I}}(t) \\ v_{\mathbf{J}}(t) \\ v_{\mathbf{K}}(t) \end{bmatrix} \tag{2.8}$$

Spherical Coordinates

In astronomy, determining the position of celestial objects is a fundamental task which is commonly represented by two coordinates: right ascension (α) and declination (δ). The right ascension is measured counterclockwise from the vernal equinox reference direction, while the declination is the angle from the celestial equator to the celestial north pole. Figure 2.1 depicts an object's right ascension and declination in the ECI Frame (2.2.3).

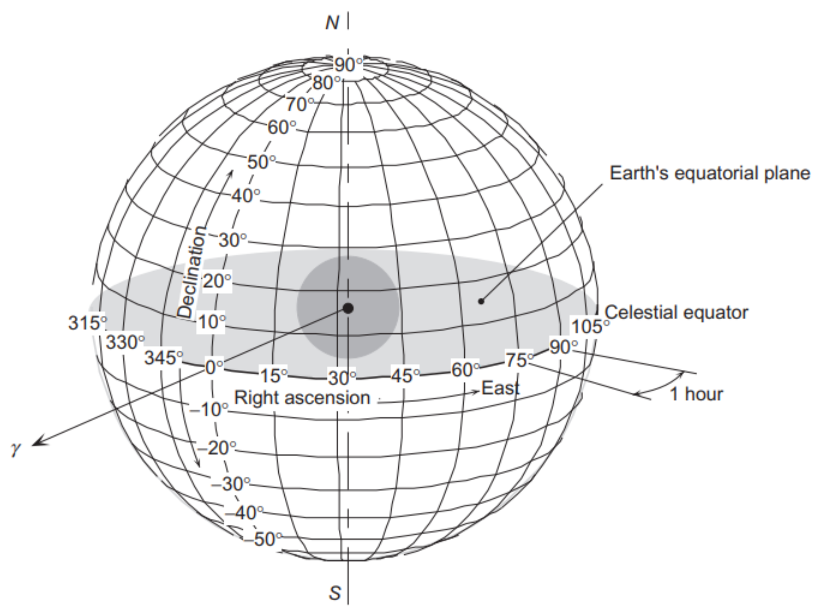

Figure 2.1: Illustration of right ascension and declination on the celestial sphere [14]

Cartesian/Rectangular Coordinates

Astronomical objects can be represented with Cartesian coordinates in the x,y, and z axis. The symbols used to measure the axis change depending on the system or model used. In Earth Centered Inertial (ECI) (Section 2.2.3) the Cartesian vectors are represented as **I**,**J**, and **K**. Figure 2.2 depicts a Cartesian right handed system commonly used in astrodyanmics.

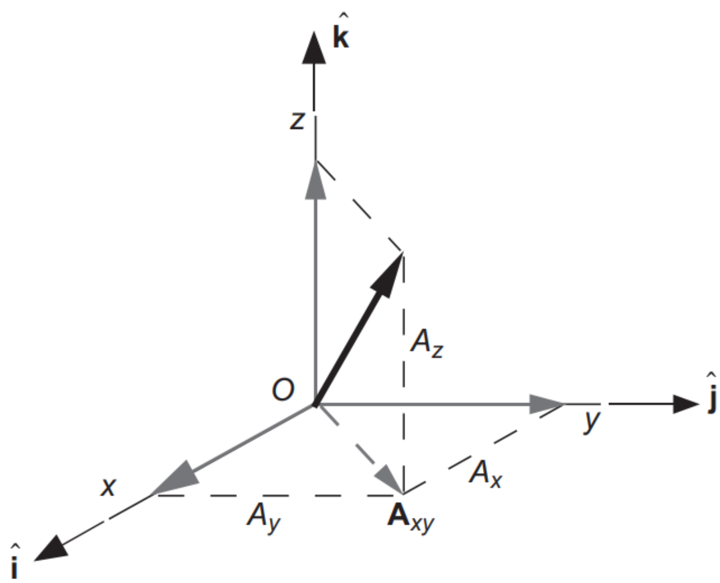

Figure 2.2: Cartesian coordinates [14]

2.2.2 Keplerian/Classic Orbital Elements (COE)

In its most basic form, an orbit can be described as two bodies spherically symmetric with point masses without internal or external perturbing forces. This simplification limits the unchanging orbital elements to only one changing parameter: time t.

Two parameters describe shape and size:

- *Eccentricity* (**e**): describes the shape of an ellipse with 0.0 describing a perfect circle.
- *Semi-major axis* (**a**): the distance between the centres of bodies in two-body orbital mechanics.

Orientation Parameters:

- *Inclination* (i): the vertical tilt of the orbital plane measured from the fundamental plane of the coordinate system.
- *Longitude of the Ascending Node* (Ω) : the angle measured counterclockwise from a reference

direction. Sometimes also referred to as the Right Ascension of the Ascending Node (RAAN) for Earth-orbiting objects.

Remaining Parameters:

- *Argument of periapsis* (ω) defines the angles from the ascension node to the periapsis of the orbit.
- *True Anomaly* (v): defines the angle between the periapsis to the celestial body at a given epoch (t).

There are several different parameters which can replace those listed above, such examples include:

- *Time of periapsis passage (T)*: the time when a satellite was at periapsis, can replace *True Anomaly* (v).
- *Longitude of perigee (*Π*)*: The angle from the reference axis **I**, to perigee. Can replace *Argument of Perigee* (ω). Calculated by: $\Pi = \Omega + \omega$

[24][15][5]

The orbital elements are described in Figure 2.3.

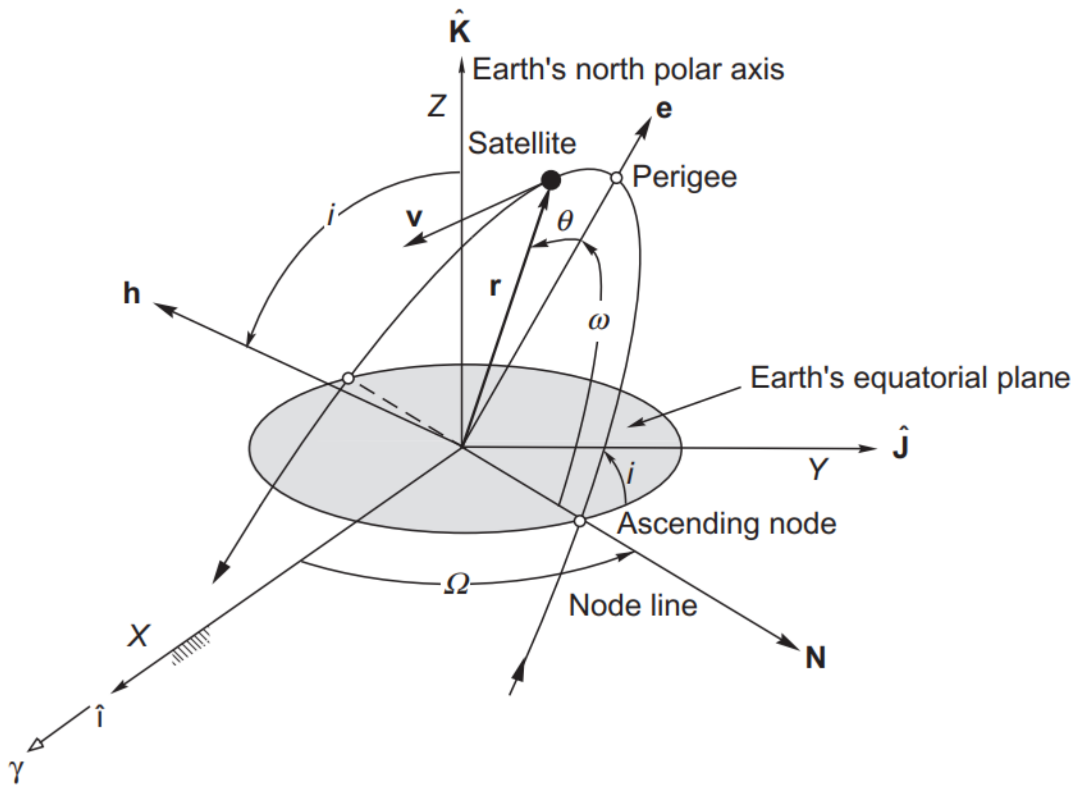

Figure 2.3: Diagram illustrating orbital elements [14]

Two Line Element

A Two Line Element (TLE) set is the standard for representing orbital data of RSOs. TLEs describe mean parameters of an object's orbit in the TEME system (Section 2.2.3) and are semi-analytically propagated using a Simplified General Perturbations (SGP) model (specifically SGP4) for propagation forward and backward in time. In addition to the six classical orbital elements listed, the mean motion rate, mean motion acceleration and drag-like parameter B^* are included in TLEs to calculate the perturbations of the RSOs motion. Similar to other ways of representing RSOs, TLEs are stated in UTC .[15]

The Table 2.1 and 2.2 describe the components of TLEs.

Line 1	
Column	Description
01	Line Number of Element Data
03-07	Satellite Number
08	Classification
10-11	International Designator (Last two digits of launch year)
12-14	International Designator (Launch number of the year)
19-20	Epoch Year (Last Two digits of year)
21-32	Epoch (Day of the year and fraction portion of the day)
34-43	First Time Derivative of the Mean Motion
45-52	Second Time Derivative of Mean Motion*
54-61	BSTAR drag term*
63	Ephemeris Type
65-68	Element number
69	Checksum(Modulo 10)

Table 2.1: Line 1 of Two Line Element Format(CelesTrack [25])

Line 2	
Column	Description
01	Line Number of Element Data
03-07	Satellite Number
09-16	Inclination [Degrees]
18-25	Right Ascension of the Ascending Node [Degrees]
27-33	Eccentricity (Leading deciemal point assumed)
35-42	Argument of Perigee [Degrees]
44-51	Mean Anomaly [Degrees]
53-63	Mean Motion [Revs/day]
64-68	Revolution number at epoch [revs]
69	Checksum (modulo 10)

Table 2.2: Line 2 of the TLE set (CelesTrack [25])

*(Leading decimal point assumed)

2.2.3 Reference Frames

The Earth Centered Inertial (ECI) System

The Earth Centered Inertial (ECI) System is a coordinate system originating at the centre of the Earth. Earth's equatorial plane is swept out as a fundamental plane with the positive X-direction pointing towards the vernal equinox while the Z-axis points towards the celestial north pole. As the north pole is constantly changing, it is important to determine an epoch and establish a standard, in this case J2000 (12 noon on January 1, 2000) is used. Figure 2.4 depict the ECI frame.

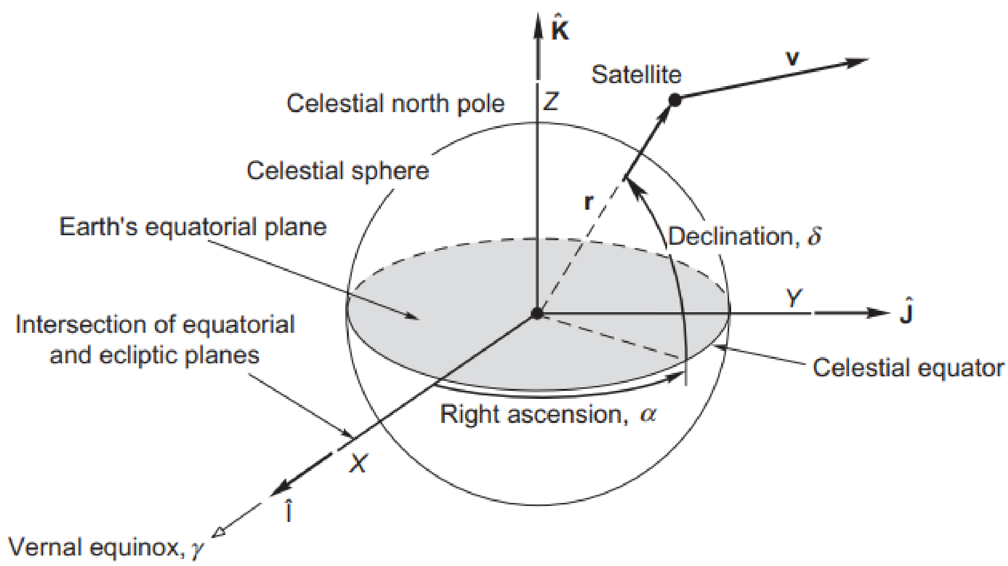

Figure 2.4: Illustration of ECI Frame [14]

True Equator, Mean Equinox (TEME)

A subset of the ECI system used for North American Aerospace Defense Command (NORAD) Two Line Element (TLE) sets and subsequently SGP4 propagators is the True Equator, Mean Equinox (TEME) frame. This frame is fixed with respect to the stars and is corrected for Earth's precession to the equinox and precession and nutation to the equator. The preferred approach is to convert TEME coordinates to something more standard, such as J2000 or the Geocentric Celestial Reference Frame (GCFR). Figure 2.5 shows the differences between the mean equator and ecliptic of date and the true equator used in the TEME frame. [15]

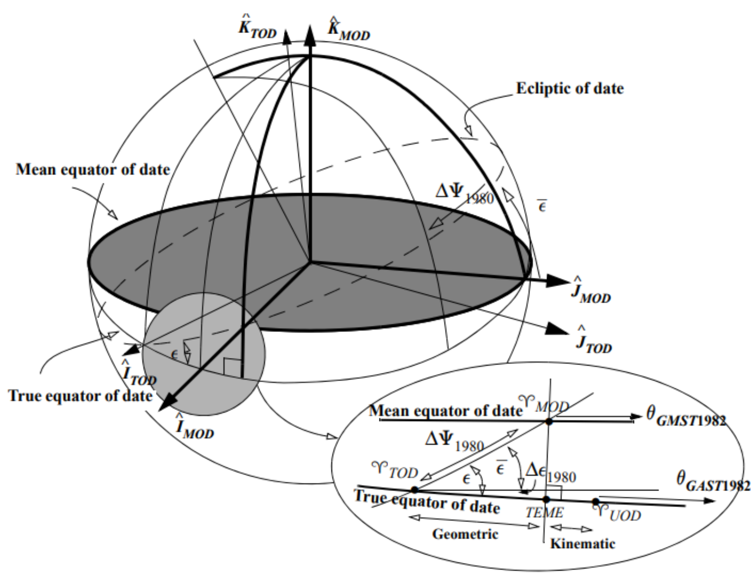

Figure 2.5: Differences between TEME frames and J200 [44]

Topocentric-Horizon Coordinate System (SEZ)

Unlike other coordinate systems, the Topocentric-Horizon Coordinate System (SEZ) System relies on the latitude and longitude of a point on Earth (Section 2.1.1). It measures positions using two angles: Azimuth (β), which is the clockwise rotation from Cardinal North, and Altitude (also known as Elevation (el)), which is the angle from the local horizon (on the reference ellipsoid) to an imaginary point directly above the observer called Zenith. In opposition to the elevation angle, the zenith angle Z is the angular distance between a celestial object and the zenith. It measures the object's height in the sky, with 0 degrees being directly overhead and 90 degrees at the horizon.

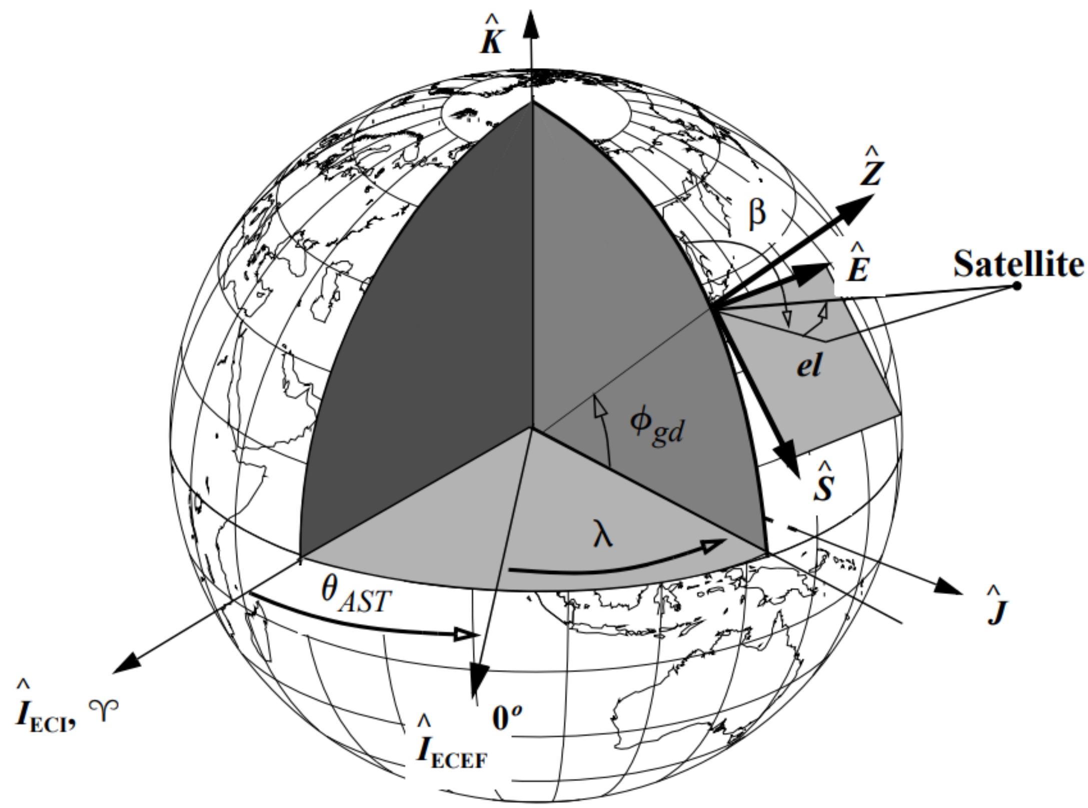

Figure 2.6: Illustration of Topocentric Frame on ECI frame [15]

Airmass Astronomy enthusiasts know that the astronomical airmass is a key factor in gauging the level of Earth's atmosphere that light from a celestial object must pass through when viewed from a specific location. This critical metric is represented by a numerical value, with lower values (approaching 1) indicating optimal viewing conditions thanks to reduced atmospheric interference. The airmass can be estimated (when the elevation angle is greater than 30 degrees) using Equation 2.9.

$$X \approx \frac{1}{cos(Z)} \tag{2.9}$$

where:

- X: Airmass
- Z: zenith angle

The error in this approximation is less than 1% for elevation angles greater than 30 degrees. [12]

2.2.4 Topocentric Equatorial Coordinate System (Inertial)

The Topocentric Equatorial Coordinate System can be thought of as a mixture of both the Topocentric-Horizon Coordinate System (SEZ) (Section 2.2.3) and the ECI frame but measured in spherical coordinates (Section 2.2.1). Although it is measured in right ascension and declination, the origin has been translated to the observer on the surface of the Earth defined by a latitude and longitude. This system is utilized more commonly by astronomers and scientists studying RSOs in Low Earth Orbit (LEO) as opposed to further objects due to the small distances between the observer and target. The topocentric right ascension is given by the variable α_t while the topocentric declination is given by δ_t [15].

2.3 Conversions between Coordinate Systems

2.3.1 Spherical to Cartesian

As noted in Section 2.2.1, the state vector in a coordinate system can be represented in both spherical or Cartesian coordinates. Converting between spherical and Cartesian coordinates is similar for both the instances of ECI and SEZ frames and is displayed in Equations 2.10-2.13:

ECI System

$$\vec{r}_{\mathbf{I},\mathbf{J},\mathbf{K}} = \begin{bmatrix} rcos(\delta)cos(\alpha) \\ rcos((\delta)sin(\alpha) \\ rsin(\delta) \end{bmatrix} \tag{2.10}$$

and

$$\vec{v}_{\mathbf{I},\mathbf{J},\mathbf{K}} = \begin{bmatrix} \dot{r}cos(\delta)cos(\alpha) - rsin(\delta)cos(\alpha)\dot{\delta} - rcos(\delta)sin(\alpha)\dot{\alpha} \\ \dot{r}cos(\delta)sin(\alpha) - rsin(\delta)sin(\alpha)\dot{\delta} + rcos(\delta)cos(\alpha)\dot{\alpha} \\ \dot{r}sin(\delta) + rcos(\delta)\dot{\delta} \end{bmatrix} \tag{2.11}$$

where *el* represents elevation in the SEZ system while β represents the Azimuth in the SEZ system.

SEZ System

$$\vec{r}_{\mathbf{S},\mathbf{E},\mathbf{Z}} = \begin{bmatrix} -\rho cos(el)cos(\beta) \\ \rho cos((el)sin(\beta) \\ \rho sin(el) \end{bmatrix} \tag{2.12}$$

and

$$\vec{v}_{\mathbf{S},\mathbf{E},\mathbf{Z}} = \begin{bmatrix} -\dot{\rho}cos(el)cos(\beta) + \rho sin(el)cos(\beta)\dot{el} + \rho cos(el)sin(\beta)\dot{\beta} \\ \dot{\rho}cos(el)sin(\beta) - \rho sin(el)sin(\beta)\dot{el} + \rho cos(el)cos(\beta)\dot{\beta} \\ \dot{\rho}sin(el) + \rho cos(el)\dot{el} \end{bmatrix} \tag{2.13}$$

where δ represents declination in the ECI system while α represents right ascension in the ECI system.

2.3.2 Elementary Rotations

Matrix formulas have been established to represent rotations on the X Y and Z axis.These are described in Equations 2.14-2.16.

$$ROT1(\theta) = \begin{bmatrix} 1 & 0 & 0 \\ 0 & cos(\theta) & sin(\theta) \\ 0 & -sin(\theta) & cos(\theta) \end{bmatrix} \quad (2.14)$$

$$ROT2(\theta) = \begin{bmatrix} cos(\theta) & 0 & -sin(\theta) \\ 0 & 1 & 0 \\ sin(\theta) & 0 & cos(\theta) \end{bmatrix} \quad (2.15)$$

$$ROT3(\theta) = \begin{bmatrix} cos(\theta) & sin(\theta) & 0 \\ -sin(\theta) & cos(\theta) & 0 \\ 0 & 0 & 1 \end{bmatrix} \quad (2.16)$$

Each rotation matrix is orthogonal, meaning that the inverse of a matrix is its transpose. For example:

$$ROT1(-\theta) = [ROT3(\theta)]^{-1} = [ROT3(\theta)]^{T} \quad (2.17)$$

[15]

2.3.3 SEZ to Earth Centered Inertial (ECI)

To calculate the position of an object in terms of ECI when SEZ data is available, Equations 2.18 to 2.24 are used.

$$\mathbf{r} = \mathbf{R} + \rho \tag{2.18}$$

At any point in Longitude and Latitude, the radius of the Earth can be described by Equation 2.19

$$\mathbf{R} = x cos(\theta_{LST})\mathbf{i} + x sin(\theta_{LST})\mathbf{j} + z\mathbf{k} \tag{2.19}$$

where:

$$x = \left[\frac{a_e}{\sqrt{(1 - e_{WGS}^2 sin^2 L)}} + H\right] cosL \tag{2.20}$$

$$z = \left[\frac{a_e(1 - e_{WGS}^2)}{\sqrt{(1 - e^2 sin^2 L)}} + H\right] sinL \tag{2.21}$$

With the rotation matrix being :

$$\tilde{\mathbf{D}}^{-\mathbf{1}} = \begin{bmatrix} sinLcos\theta_{LST} & -sin\theta_{LST} & cosLcos\theta_{LST} \\ sinLsin\theta_{LST} & cos\theta_{LST} & cosLsin\theta_{LST} \\ -cosL & 0 & sinL \end{bmatrix} \tag{2.22}$$

Example converting vector $\vec{r}_{I,J,K}$ to $\vec{r}_{S,E,Z}$:

$$\begin{bmatrix} r_I \\ r_J \\ r_K \end{bmatrix} = \tilde{\mathbf{D}}^{-\mathbf{1}} \begin{bmatrix} r_S \\ r_E \\ r_Z \end{bmatrix} \tag{2.23}$$

For velocity, this is Equation 2.24:

$$\mathbf{v} = \dot{\rho} + w \times \mathbf{r} \tag{2.24}$$

This can also be expressed in the form of General Rotation Matrices as:

$$\vec{r}_{I,J,K} = ROT3(-\theta_{LST})ROT2(-90^o - L))\vec{r}_{S,E,Z} \tag{2.25}$$

[15]

- **R**=Radius of the Earth at a given latitude and longitude
- **r**=position vector in ECI coordinates
- ρ:Range in SEZ coordinates
- H:Height above sea level
- L:Geodetic latitude
- e_{WGS} : Eccentricity of the reference ellipsoid
- a_e:Semi-major axis of the Earth
- w : the angular velocity of Earth

2.3.4 Earth Centered Inertial (ECI) to Topocentric-Horizon Coordinate System (SEZ)

Reversal of the rotations and applying a transformation will then result in the topocentric coordinates as described in Equation 2.26 and Equation 2.27.

$$\tilde{\mathbf{D}} \begin{bmatrix} r_I \\ r_J \\ r_K \end{bmatrix} = \begin{bmatrix} r_S \\ r_E \\ r_Z \end{bmatrix} \tag{2.26}$$

$$\vec{r}_{SEZ} = ROT2(90^o - L)ROT3(\theta_{LST})\vec{r}_{IJK} \tag{2.27}$$

2.3.5 Topocentric Equatorial to Earth Centered Inertial System

Since the topocentic equatorial system is parallel to the ECI system, only a translation must be made to convert from one frame to another, as seen in Equation 2.28 and 2.29.

$$\vec{r}_{ECI} = \vec{\rho}_{ECI} + \vec{r}_{SiteECI} \tag{2.28}$$

$$\vec{v}_{ECI} = \vec{\dot{\rho}}_{ECI} + \vec{v}_{SiteECI} \tag{2.29}$$

Utilizing Spherical Coordinates

The vectors describing an orbit may also be converted directly into spherical coordinates with Equations 2.30 to 2.32 [15].

$$sin(\delta_t) = sin(el)sin(\mathbf{L}) + cos(el)cos(\mathbf{L})cos(\beta) \tag{2.30}$$

$$sin(LHA) = -\frac{sin(\beta)cos(el)cos(\mathbf{L})}{cos(\beta_t)cos(\mathbf{L})} \tag{2.31}$$

$$\alpha_t = \theta_{LST} - LHA \tag{2.32}$$

- α_t : Topocentric Right Ascension
- δ_t : Topocentric Declination
- LHA: Local Hour Angle

2.3.6 State Vector to Two Line Element (TLE)

TLE sets contain *mean* orbital elements for an RSO, while state vectors contain osculation patterns at a given epoch. This means an iterative process utilizing the SGP4 algorithm must be used along with an initial mean guess of the orbital elements to approximate a TLE set. This is explained further in *Fundemental of Astrodynamics* [5]. Furthermore *Fundementals of Astrodynamics and Applications* Vallado [15] presents multiple ways to predict perturbation parameters required for created TLE sets.

2.3.7 Two Line Element (TLE)s to Classic Orbital Elements (COE)

TLE sets for most low-precision applications can be used directly as COE if the desired epoch for the orbital elements is similar to the epoch stated in the TLE. Conversely, if the desired time for the orbital elements is much different than that of the TLE set, one can propagate the TLEs forward or backwards to get the desired time with significant growth in error beyond a few days, especially with unknown BStar terms [5].

2.4 Observing RSOs

Observing an RSO can be completed with many types of sensors. Optical sensors offer a much greater range over passive radar but are limited to only offering angular measurements. The focus of this research was placed on optical measurements, following astronomy standards.

2.4.1 Flexible Image Transport System (FITS) Images

In astronomical practices, the .FITS file is used extensively to capture images of celestial bodies while also storing important meta-data of the target and observer. The data required for image processing include values such as the gain of the sensor, latitude and longitude of the observer, the bounds of the overscan region of the sensor, the filters used, exposure time, and observation times. [35]

2.4.2 Astrometry

Astrometry describes the whereabouts of a given RSO. The values of topocentric right ascension and declination are typically used to describe the RSO by comparing it to the background starfield: a process known as plate solving.

Plate Solving

When catalogued celestial bodies are measured, their pixel locations (centroids) can be used to plate-solve the image, producing World Coordinate System (WCS) information. With WCS information, the pixel location of the light sources is matched to their celestial coordinates (in right ascension and declination). Plate solving can be completed by both nova.astrometry.net [27] and with external software such as Visual Pinpoint [16]. WCS information is saved within the .FITS headers when an

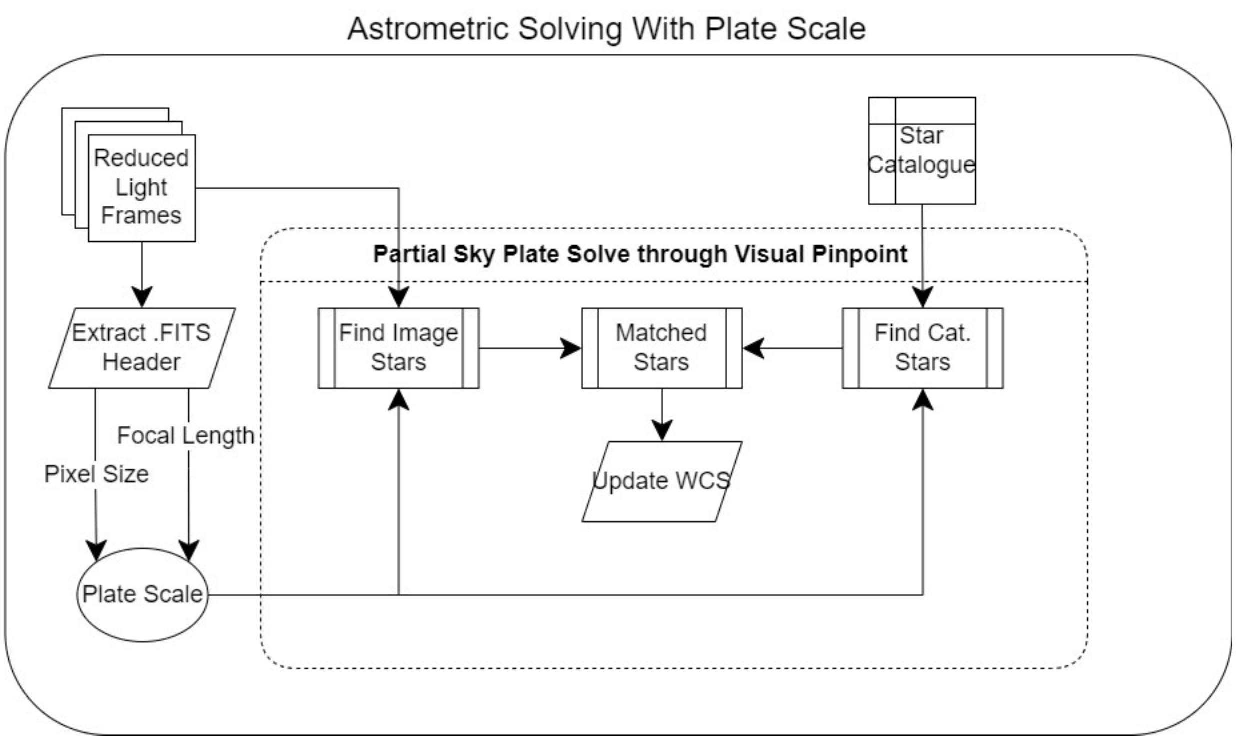

Figure 2.7: Visual Pinpoint Plate Solving Flow chat

image is plate solved. While nova.astrometry.net can 'blindly' plate solve an image without any plate scale (Figure 2.8), other software such as Visual Pinpoint cannot (Figure 2.7).

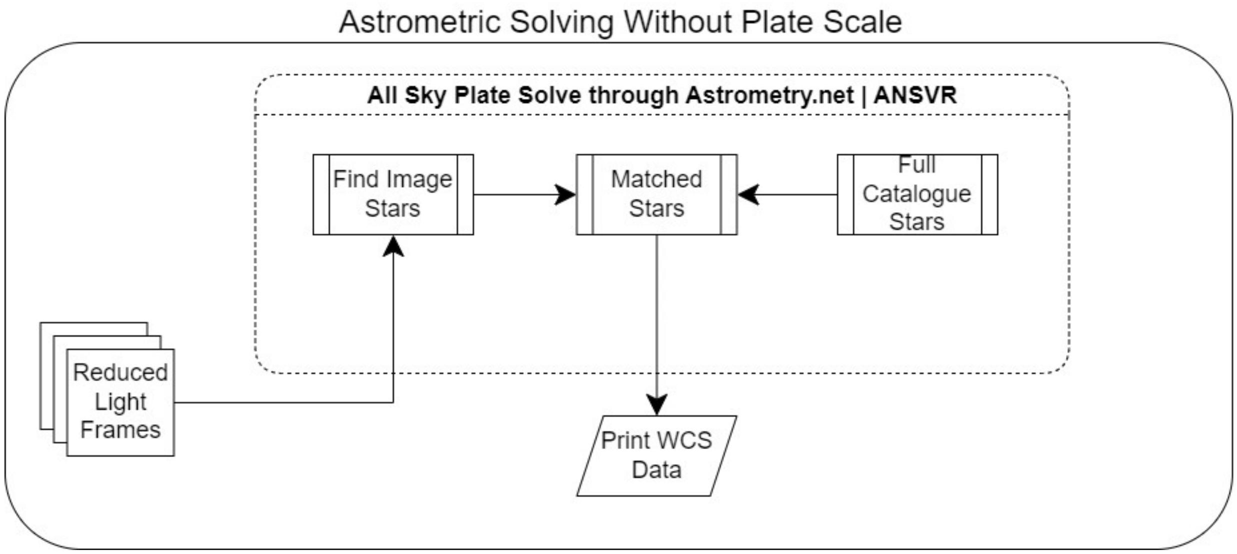

Figure 2.8: Plate Solving without Plate Scale

Recording Distortions

The Simple Imaging Polynomial (SIP) convention is used to describe the distortions seen in the image and is saved in the .FITS headers. When an image is plate solved (see Section 3.5.3), the distortions are saved with the suffix '-SIP' in the .FITS keyword. While the CRPIX*n* represents the reference pixel from which the distortions are calculated, the CD*n_m* keywords encode skew as well as rotation and scaling. Quadratic or higher order terms of the distortion polynomial are represented by functions $f(u,v)$ and $g(u,v)$. u,v are relative pixel coordinates with the origin at CRPIX1 and CRPIX2 and x,y are "intermediate world coordinates" in degrees with the origin at CRVAL1 and CRVAL2. [39] [40]

$$\begin{pmatrix} x \\ y \end{pmatrix} = \begin{pmatrix} CD1\_1 & CD1\_2 \\ CD2\_1 & CD2\_2 \end{pmatrix} \begin{pmatrix} u + f(u,v) \\ v + g(u,v) \end{pmatrix} \tag{2.33}$$

Other coefficients are complemented by keywords like A_ ORDER, B_ ORDER, A_ COEFF, B_ COEFF, PV1_ 1, PV1_ 2, PV2_ 1, and PV2_ 2.

Star Catalogues

The act of Plate Solving a frame requires the use of a star catalogue; a set of recorded stars that have been transformed and recorded into a standard format. Different star catalogues have different advantages. For the application of photometry the American Association of Variable Star Observers Photometric All-Sky Survey (APASS) [20] star sub-catalogue, part of the The Fourth US Naval Observatory CCD Astrograph Catalog (UCAC4) [48] is the most extensive photometric catalogue to date. Traditional standard photometric calibration fields such as Landolt stars [26] also exists in these catalogues. Regardless of the catalogue used, recorded magnitudes of stars in the Jousin-Cousins or The Sloan Digital Sky Survey (SDSS)[46] standard colour systems are required for transforming instrumental magnitude to apparent magnitude on a standard system. The VizieR service can be leveraged to call on available catalogues to retrieve stars given a certain right ascension and declination. To match catalogue stars up with an image's, the image must be plate solved and the VizieR service used to query surrounding stars which are then matched with a proximity correlation.

2.4.3 Data Reduction

The Handbook of Astronomical Image Processing [7] discusses a variety of topics relevant to processing images. Leveraging the *AstroPy ccdproc* library [13] the *CCD Data Reduction Guide* [30] depicts the steps required to pre-process images captured by an optical or near-infrared sensor. The pre-processing/data reduction pipeline is seen in Figure 2.9, 3.20, and 2.10. The process requires capturing of Bias, Dark and Flat frames. Bias frames display the produced noise floor at an instantaneous exposure time, while Dark frames are images of the noise at the same exposure time as the light frames (images of light sources). Flat frames, are frames of uniform light that are used to divide out dust particles and other artifacts from the light frames. Some sensors, such as NEOSSat, contain noise in a sinusoidal wave like pattern. This pattern is identified with the use of a Fourier analysis and then subtracted from the image.

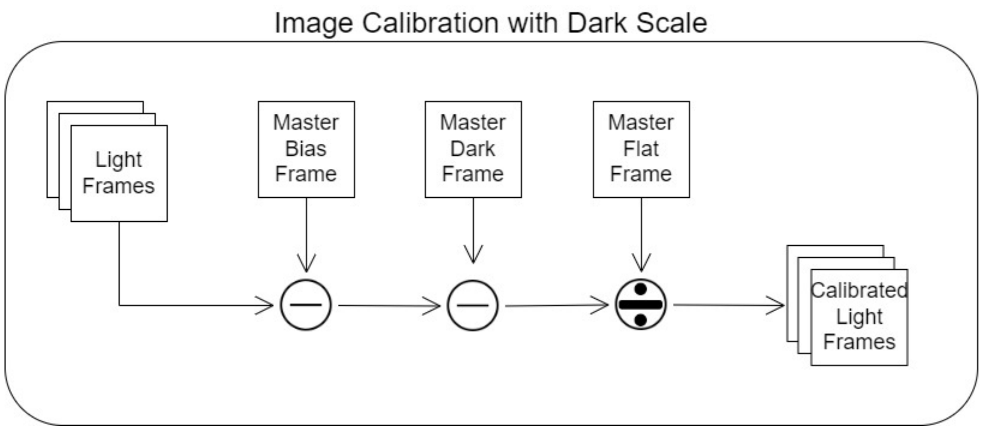

Figure 2.9: Generalized Image Reduction pipeline

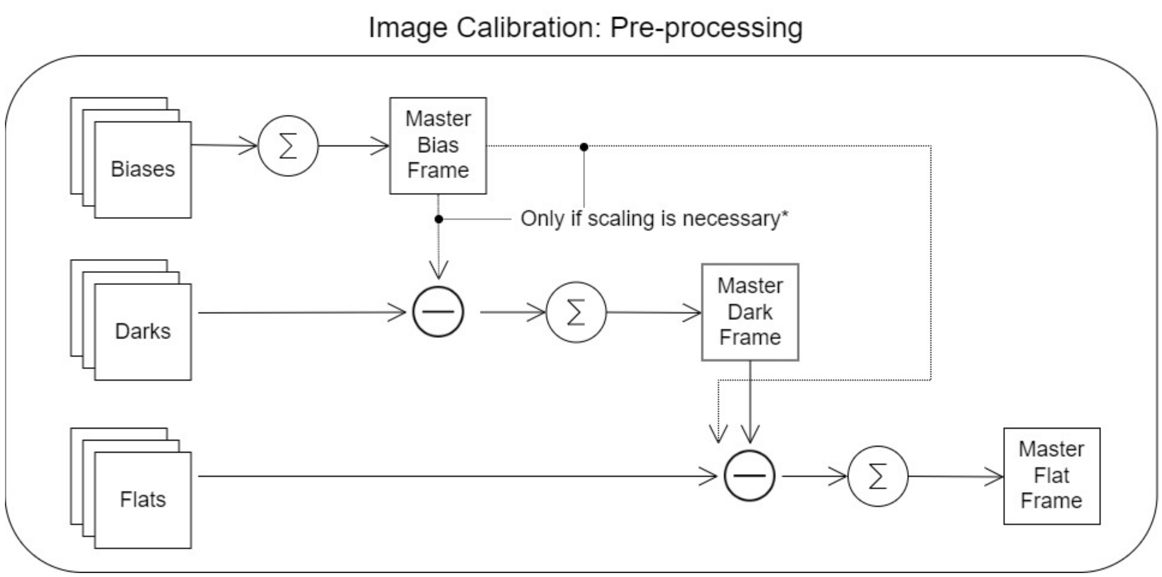

Figure 2.10: Calibration Frame creation

*Scaling is necessary if the dark frames exposure time and flat frames exposure time is extremely different. The master dark frame is multiplied by the exposure time to meet that of the flat frame.

2.4.4 Photometry

Photometry is the act of measuring the light received from an object, whether it be a star, galaxy or RSO. *Astronomical Photometry* by Henden and Kaitchuck [21] is the primary book for understanding and measuring celestial light sources. The book covers photometric systems, data reductions, observation calculations, and observing techniques. Atmospheric distortions and sensor specific characters cause measurement errors in the light received from an Earth-bound observer. To calibrate the data into a standard system, methods such as absolute photometry and differential photometry must be enforced for ground-based observations. Meanwhile exo-atmospheric calibration, such as is the case for NEOSSat, is simplified and only requires a zero-point offset value. Originally published in *Astrometric Techniques* [22] in 1962 the methods for producing transformations have been around for many years. Modern implementations of these transformations are seen in The *CCD Photometric Calibration Cookbook* [34] with applications to asteroids seen in Warner's *A Practical Guide to Light curve Photometry* [1]. After the data has been reduced, photometry starts with measuring the background of the image and subtracting it. The light sources in the images are then detected. An aperture (for aperture photometry) is then chosen using the Signal-to-noise ratio (SNR), and the aperture is corrected for. For this, the absolute photometry or differential photometry equation is used to produce a calibrated reading of the light source.

Measuring Image Backgrounds

Estimating the background noise around a RSO can be accomplished in many ways. The simplest method involves calculating the mean or median of a given image and subtracting the average value from the (input) science image. Source Extraction and Photometry Package (SEP) offers a more dynamic approach to background estimation, switching between mean or median usage depending on the sigma values of the light sources. [8].

Aperture Photometry

After estimating and subtracting the background from the images, the sources in the image must be detected. There are three common techniques for light source detection: the SEP, PhotUtils, and Image Reduction and Analysis Facility (IRAF) DAOPhot. Each technique detects the light sources in an image in slightly different ways. After detecting the stars in a test image the Signal-to-noise ratio (SNR) of the light sources in the image is measured iteratively with increasing aperture sizes to find the optimal aperture size to conduct aperture photometry. The Signal-to-noise ratio (SNR) equation is defined by Equation 2.34 below. [23]

$$\frac{S}{N} = \frac{t * B * G}{\sqrt{t * (B * G + n_{pix} * (Sky * G + D)) + n_{pix} * (R * G)^2}} \tag{2.34}$$

Where:

- t: The exposure time of the image in seconds
- B: The brightness of the light source in ADU/second
- G: The effective gain of the sensor in e^-/ADU
- n_{pix}: The number of pixels in the aperture
- Sky: The background sky brightness in ADU/second
- D: Dark current created by thermal noise in ADU/second/pixel
- R: Read noise in ADUs

An issue arises with choosing an aperture to get the optimal SNR: the optimal aperture leaves out some signal from the source. To compensate for this, an aperture correction term is introduced. This value is derived from finding the asymptotic aperture magnitude for a series of bright stars and calculating the difference between the asymptotic aperture magnitude and the aperture magnitude at the chosen optimal radius. If the sky conditions are photometric (< 2% transparency variation) then the same optimal aperture radius and aperture correction value can be used for the entire dataset. Each filter will require its own aperture correction value. The equations for deriving the instrumental magnitude from the aperture magnitude is seen in Equation 2.35 and 2.36

$$m_{aperture} = -2.5 * log_{10}(S) \tag{2.35}$$

$$m_{instrument} = m_{aperture} - C \tag{2.36}$$

where:

- S: the Flux of the Source (ADU/sec)
- $m_{aperture}$: the aperture flux (mags)
- C: Aperture Correction (mags)
- m_{instr}: instrumental magnitude (mags)

The variance of the measured signal must also be considered. Equation 2.37 was used to calculate this metric. [23]

$$\sigma_{m_{instr}} = 2.5 log_{10}(e) \frac{N}{S} \tag{2.37}$$

where:

1. N: the noise associated with the source
2. S: the signal associated with the source
3. e: Euler's number
4. $\sigma_{m_{instr}}$: standard error of the instrumental magnitude

The Absolute Photometry Equation

Absolute photometry requires viewing catalogued stars at various airmasses with a wide range of colours. It is a general rule in astronomy to never observe below 30 degrees elevation [31]. At these angles, the estimation for airmass as seen in Equation 2.9 dissolves, and a much more intensive model is required to estimate the airmass' effect on the observations. Additionally, the second-order extinction coefficient becomes much larger (as is seen when the sun appears red just above the horizon at sunset). Observations of standard stars can be done in between observations of the target celestial body. The Landolt catalogue stars [26] in the UBVRI Johnson Cousins filters are typically used.

The absolute photometry equation is described in Equation 2.38.

$$V = v - k_v' X + T_v(CI) + ZP_v \tag{2.38}$$

- V: reduced standard V magnitude
- v: instrumental magnitude in V filter
- k_v' : first-order extinction in V
- X: airmass at the time of the observation
- T_v: transformation for V filter
- CI: Standard colour index (B-V)
- ZP_V: nightly zero-point for V filter

Absolute photometry requires three main calculations: colour transformation calculations (to find t_v), extinction coefficient calculations (to find k_v') and an apparent colour index.

Colour Transformation

The colour transformations are calculated by matching the observed stars for a standard starfield to their respective catalogue values. When this has occurred, the calculated apparent colour index is plotted against the apparent magnitude of a star minus it's instrumental magnitude. A linear least fit is taken of this plot and the slope and error is taken. The slope represents the colour transformation required for Equation 2.38.

Extinction Coefficients

Extinction coefficients are found by plotting the apparent magnitude minus the instrumental airmass on the y-axis against the airmass on the x-axis. A wide range of airmasses should be observed. From this a linear least squares fit is made to the data and it's resultant slope is the combined extinction coefficients required for Equation 2.38. [1]

Colour Index

The apparent colour index can be estimated by fitting a linear least squares fit against a plot of the instrumental colour index and the apparent colour index. The apparent colour index for any given light source is equal to the instrumental colour index minus the extinction multiplied by the airmass plus the zeropoint. Equation 2.39 shows this relationship. [1]

$$CI = (ci - k'X) + ZP \tag{2.39}$$

Where:

- : Apparent Colour Index
- : Instrumental Colour index
- : Extinction Coefficient

- : Nightly Zeropoint

Differential Photometry

When imaging RSOs if there are a sufficient number of catalogue stars (>4) in the background of the RSO images then those stars can be used to calibrate each image and RSO within it to a standard. With less than 4 catalogued stars, the image cannot be plate solved while with more than 4 stars, the standard deviation of the estimated standard magnitude is reduced. The differential photometry equation is described by Equation 2.40.

$$\Delta M = (m_o - m_c) + T * (CI_o - CI_c) \tag{2.40}$$

- ΔM: differential magnitude in a standard color
- m_o: instrumental magnitude of target
- m_c: instrument magnitude of comparison
- T: transform for given filter
- CI_o:standard color index for target, e.g., (V-R)
- CI_c: standard color index for comparison, e.g., (V-R)

The apparent magnitude can then be calculated using the catalogued standard magnitude of comparison stars and the colour index (Equation 2.41).

$$M = \frac{(\sum_{j=1}^{N} (M_c + \Delta M)_j)}{N} \tag{2.41}$$

- M: reduced standard magnitude of target
- M_c: standard magnitude of comparison

- ΔM: standard differential magnitude (object-comparison)
- N: number of comparison stars used

Exo-atmospheric Transformations

Without the concern of the atmosphere, calibrating the measurement of the instrumental magnitude simplifies to subtracting the matched stars' instrumental magnitude from their catalogue magnitudes to calculate a zeropoint (Equation 2.42).

$$V = v - Zp \tag{2.42}$$

- V: visual magnitude
- v: instrumental magnitude
- Zp: Zeropoint

The described equations in these texts are applied to other celestial bodies such as comets, but the application to RSO has not been previously explored. The processing pipeline for exo-atmopsheric is described in Figure 2.11.

2.5 Examples in Literature

2.5.1 Ground-based observations of RSOs

Rough calibration techniques are seen in *Time-Resolved visible/near-infrared spectrometric observations of the Galaxy 11 geostationary satellite* [38] with non-filter observations. Catalogue stars are typically recorded in either Johnson-Cousins or SLOAN filter sets, thus being improperly

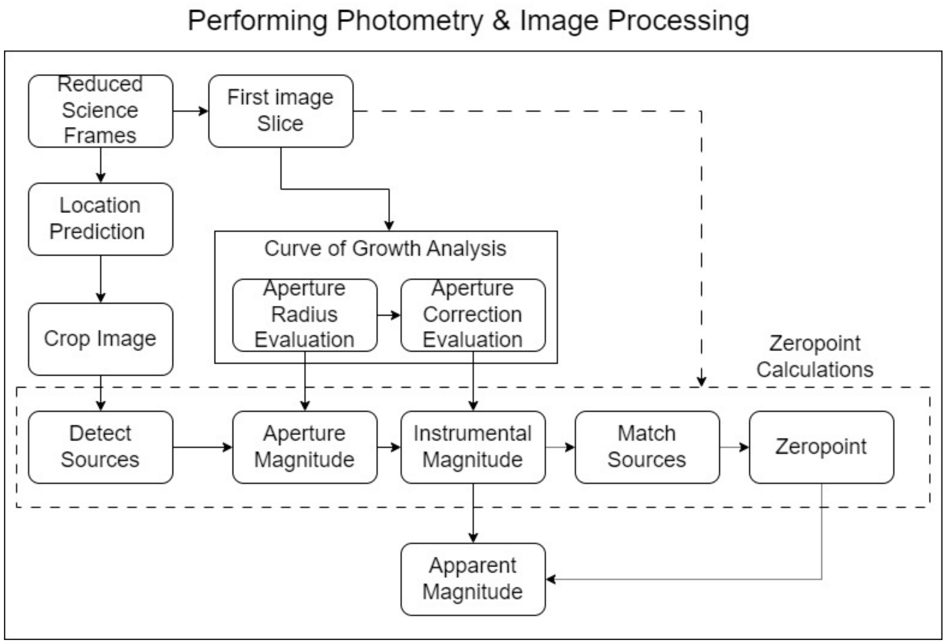

Figure 2.11: The exo-atmopsheric photometry pipeline

compared to their instrumental values. Other studies don't take into consideration atmospheric distortions caused by airmass and the difference in filters used and will only calculate a zeropoint as opposed to performing differential or absolute photometry.

2.5.2 Near-Earth Object Surveillance Satellite (NEOSSat)

Canada stands at the forefront of SSA research with NEOSSat being the world's first space telescope dedicated to High Earth Orbit Space Surveillance (HEOSS), with specific tracking for NEOs and RSOs. In *Key Findings from the NEOSSat Space-Based SSA Microsatellite Mission* [41], the authors address observing GEOs from NEOSSat's LEO orbit of 700km altitude. Additionally, *Combined Space-Based Observations of Geostationary Satellites* [37] provides some background on performing SSA from the sensor. A rough photometric calibration with NEOSSat is used with a preset zeropoint of 21.0 and the data is distance normalized.

2.6 Gaps in Research & Contributions

While there is a standardized pipeline for performing photometric transformations on celestial objects, limited literature exists for performing photometry on RSOs. The few photometric studies that have been performed on RSOs have used instrumental magnitudes as opposed to absolute or apparent magnitudes, limiting their usefulness when comparing them to other sets of data. Additional gaps in research include space-based sensor observations being largely limited to GEO satellites and focusing on astrometry to update orbits rather than photometry.

The research performed in this project addresses the gaps in research by placing importance on photometric transformation of RSOs and looks at cis-lunar object tracking and observation from space-based sensors. The goal of this research was to develop the tools required for performing advanced photometric techniques.

Chapter 3

Methods

The research conducted made use of three datasets: IntelSat 10-02 was imaged in the winter of 2022 in St. Johns Newfoundland, AnikF1 was imaged in Ottawa in the summer of 2022 and JWST was imaged by NEOSSat in the winter of 2023. Each dataset looks at different techniques for acquiring calibrated light curves: absolute photometry is used for the IntelSat 10-02 data, differential photometry is used for the AnikF1 dataset and a simplified zeropoint calculation is used to measure JWST imagery. The measurements and findings of IntelSat 10-02 and JWST were previously used for CASJ 2022 and Advanced Maui Optical and Space Surveillance Technologies (AMOS) 2023.

3.1 Target Resident Space Objects

3.1.1 Motivation

Intelsat 10-02

The successful docking of Northrop Grumman's MEV-2 satellite with Intelsat 10-02 in geosynchronous orbit on April 12, 2021, marked a groundbreaking achievement in satellite servicing technology. This innovative feat extended the satellite's service life but also provided scientists

Figure 3.1: Celestron scope used to capture AnikF1 data in-situ

with a unique opportunity to measure a docked satellite. By extracting the calibrated light curve of Intelsat 10-02 with MEV-2, it becomes easier to compare it with other GEO satellites with similar bus types and previously captured light curves. Although a detailed comparison of Intelsat 10-02 light curves is beyond the scope of this thesis, the processes used to extract the data are relevant to the rest of the work conducted.

AnikF1

During August 2022, the Stratos-Science campaign successfully launched multiple research payloads up to 40km high to study atmospheric conditions and imaging. Among these payloads, the RSOnar mission, led by York University, primarily focused on investigating a dual-purpose star tracker. As part of the mission, the payload was briefly directed to observe domestic satellites, including AnikF1, while the ground segment involved comparing resulting light curves from both sensors.

JWST with NEOSSat

As of early 2023, the JWST was actively functioning near the Earth-Sun Lagrange Point (L2). As it moved closer to Earth (Figure 3.2), its brightness grew, rendering it detectable by more compact sensors. Given that Canada is the sole country equipped with an SSA research satellite, NEOSSat, JWST presented an exceptional chance to advance our comprehension of image processing for objects situated within the cis-lunar orbital regimes.

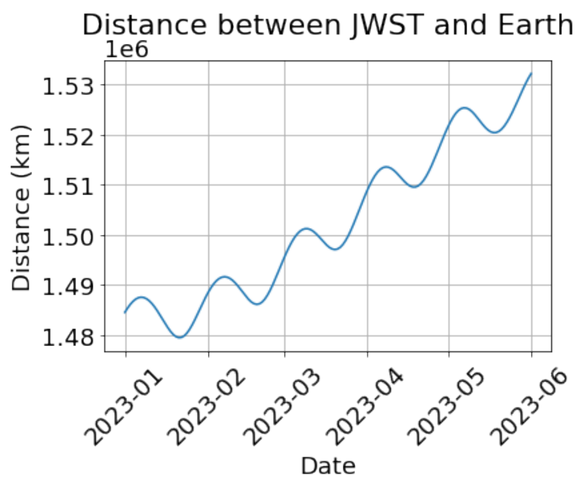

Figure 3.2: Calculated JWST distances

3.1.2 Characteristics

JWST

JWST is positioned at L2, the second Lagrange point because it offers a stable and unobstructed location far from Earth's interference and the Sun's heat, ideal for its primary mission of conducting precise infrared observations of the universe. L2's cold, dark environment naturally cools the telescope's instruments to the required temperatures for detecting faint infrared signals. Figure 3.3 shows the orbit of JWST for 2022 and the first half of 2023.

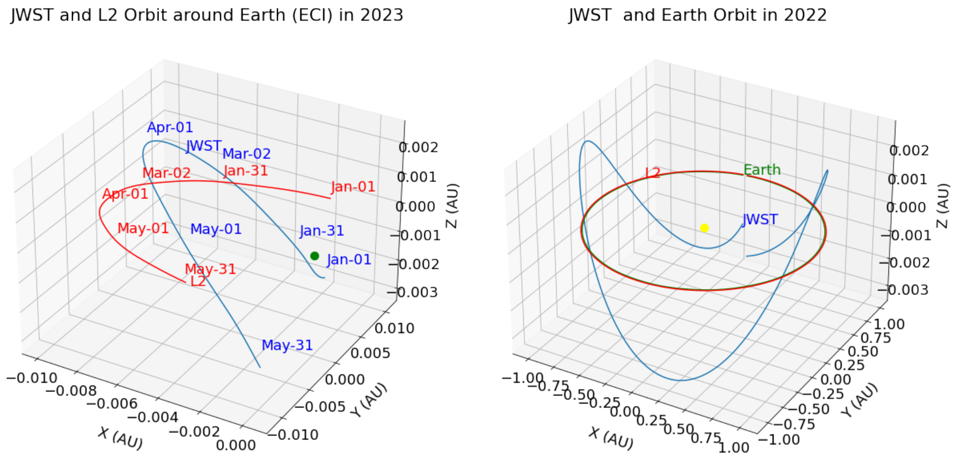

Figure 3.3: JWST's orbit (left: 2023) (right: 2022)

GEO RSOs

The IntelSat 10-02 and AnikF1 communications satellites are strategically placed at different RAANs to ensure optimal coverage for their intended regions. While IntelSat 10-02 primarily services Europe and parts of Africa, AnikF1 is designed to provide coverage in Central and North America. This positioning ensures that both satellites can effectively service their respective areas, as illustrated in Figure 3.4.

The azimuth, elevation and airmass or AnikF1 is seen in Figure 3.5.

Figure 3.6 displays the Azimuth and Elevation of IntelSat 10-02 from St. John's Newfoundland. The Elevation for IntelSat 10-02 is below 20 degrees, indicating a more challenging airmass for potential observations.

The recorded airmasses of IntelSat 10-02 are seen in Figure 3.7. These recorded airmasses do not increase or decrease with time, and thus are probably recorded incorrectly.

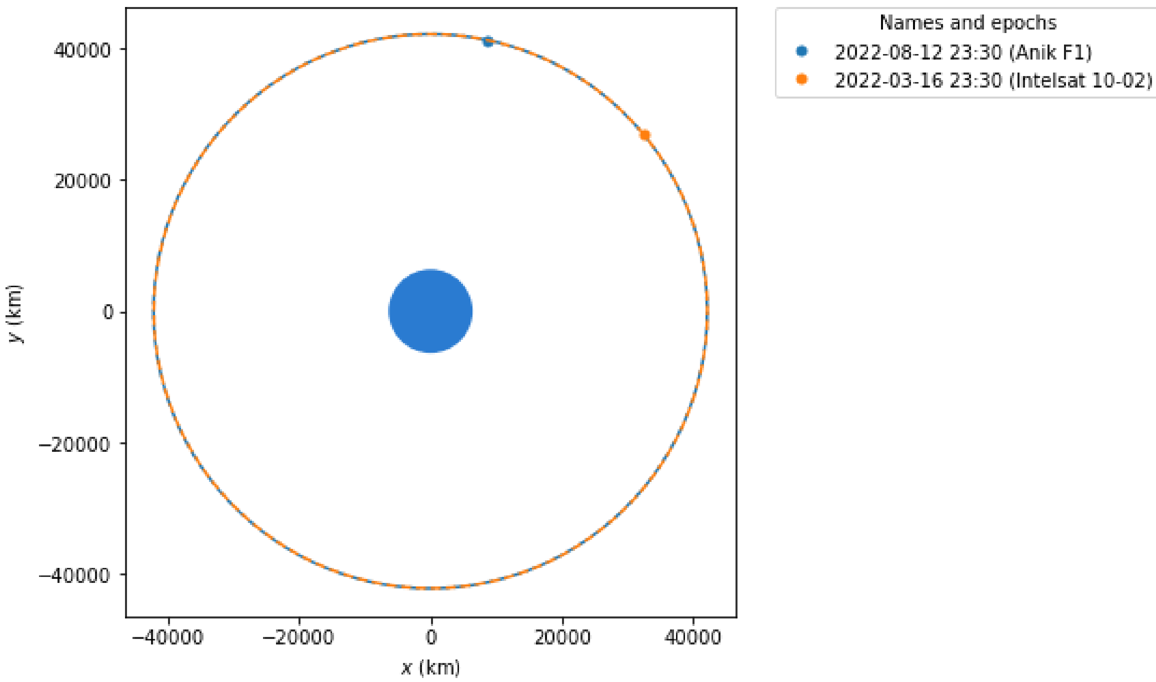

Figure 3.4: Orbit of AnikF1 and IntelSat 10-02

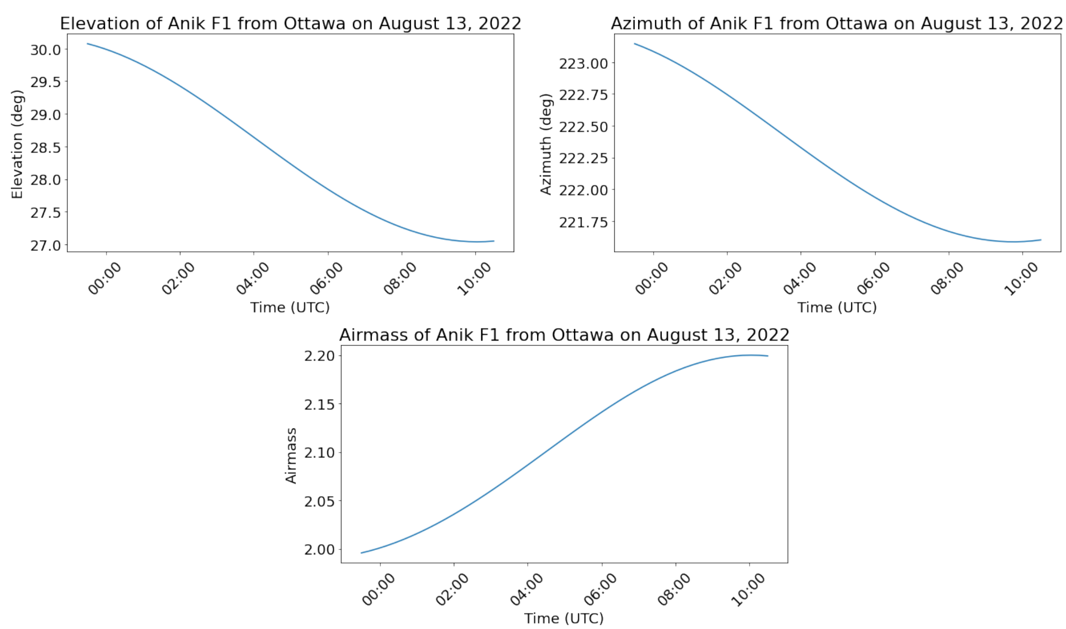

Figure 3.5: Elevation, azimuth and airmass of AnikF1

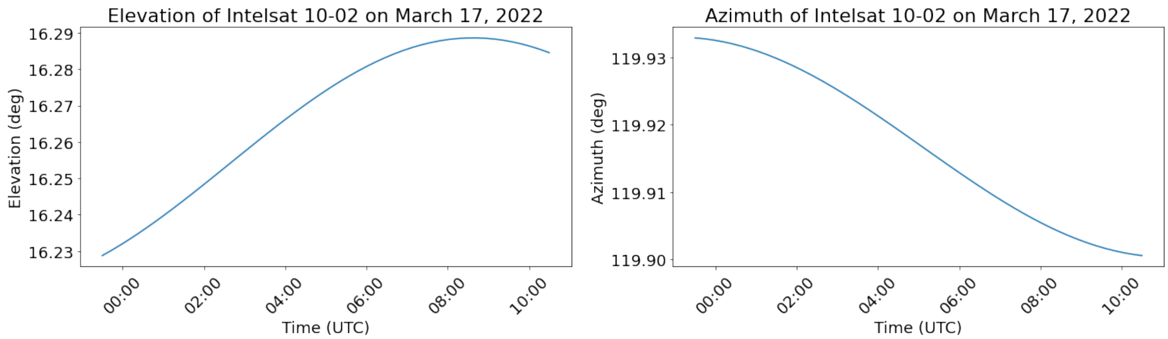

Figure 3.6: Simulated elevation and azimuth of IntelSat 10-02

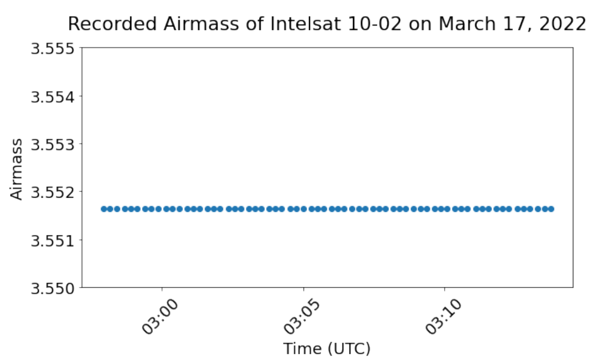

Figure 3.7: Recorded IntelSat 10-02 airmasses

3.2 Prediction

Observations of RSOs were planned in accordance to background star density. Figure 3.8 displays the observation windows of three satellites, the aforementioned IntelSat 10-02 observations on March 16 2022, and observation of Anik F1 on August 13 2022. The observation of Anik F1 would pass through a relatively high density of stars in the APASS catalogue (containing Landolt stars) allowing for differential photometry to be performed. Additionally JWST is plotted over the star density, but due to it's relative motion, long integration time exposures can be made allowing for detection of fainter stars.

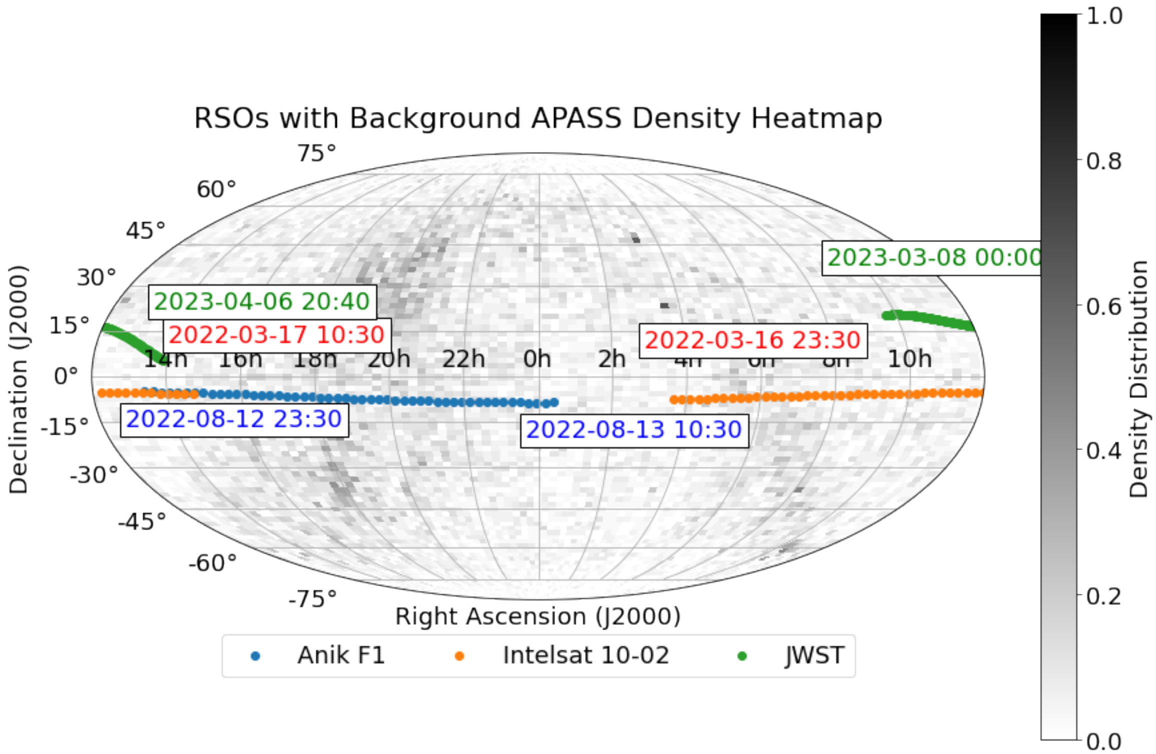

Figure 3.8: Satellite observations superimposed on APASS catalogue heatmap

3.2.1 Geosynchronous Equatorial Orbit (GEO) Predictions

The estimated positions of the GEO objects were made by propagating the satellite's TLE at a nearby epoch backward or forward in time. Look angles (azimuth and elevation) were calculated by first propagating a TLE and then converting the state vector in TEME to SEZ. The created pipeline pulled on *Skyfield*'s API for TLE propagation [36].

Finder Images

Multiple Digitized Sky Survey (DSS) images were rendered with *astroplan* with the desired epochs to show what the approximate background sky would look like for each image captured. This finder image predcitions are seen in Figure 3.9.

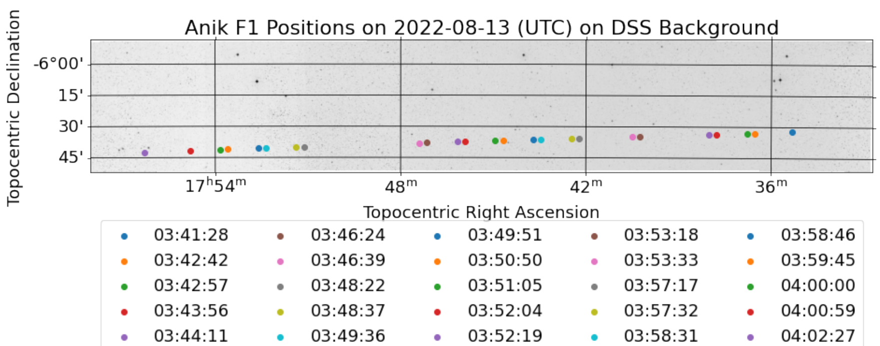

Figure 3.9: Estimated Anik F1 positions

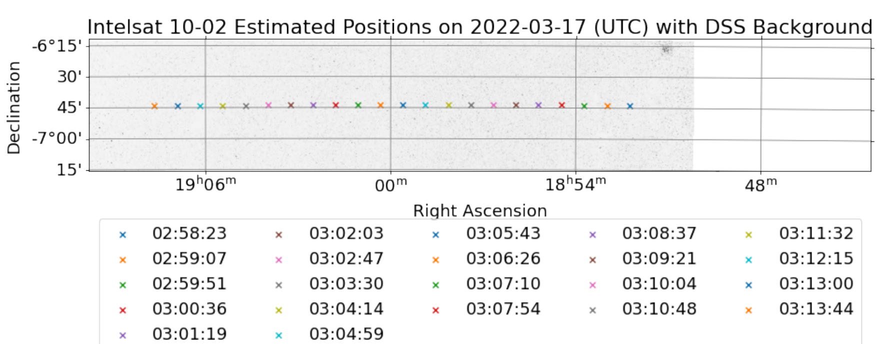

Figure 3.10: Estimated IntelSat 10-02 positions

Starfields

Observing Figure 3.8 and 3.10, IntelSat 10-02 does not contain a sufficient amount of bright catalogue stars in the background of the observations, thus limiting differential photometry capabilities and requiring absolute photometry with equation 2.38. The *AstroPy astroplan* module was used to produce visualizations for comparing different star fields throughout a given night given the starfields right ascension and declination. Figure 3.11 shows an example of one such visualization: the SA 23 starfield was chosen based on its visibility and change in airmass during the observation period.

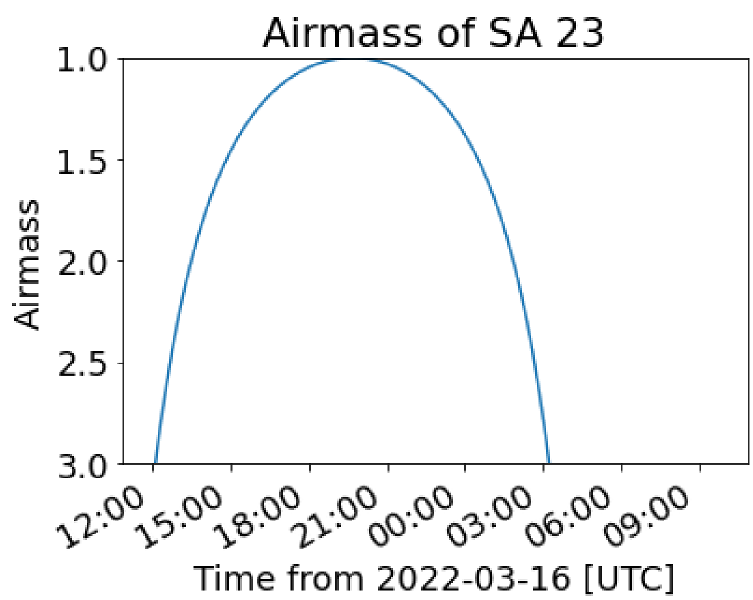

Figure 3.11: Airmass of the SA 23 starfield used for absolute photometry

3.2.2 JWST Prediction

Due to the complexities of capturing JWST with another satellite, a flowchart describing the predictions of the satellite was created. This is depicted in Figure 3.12.

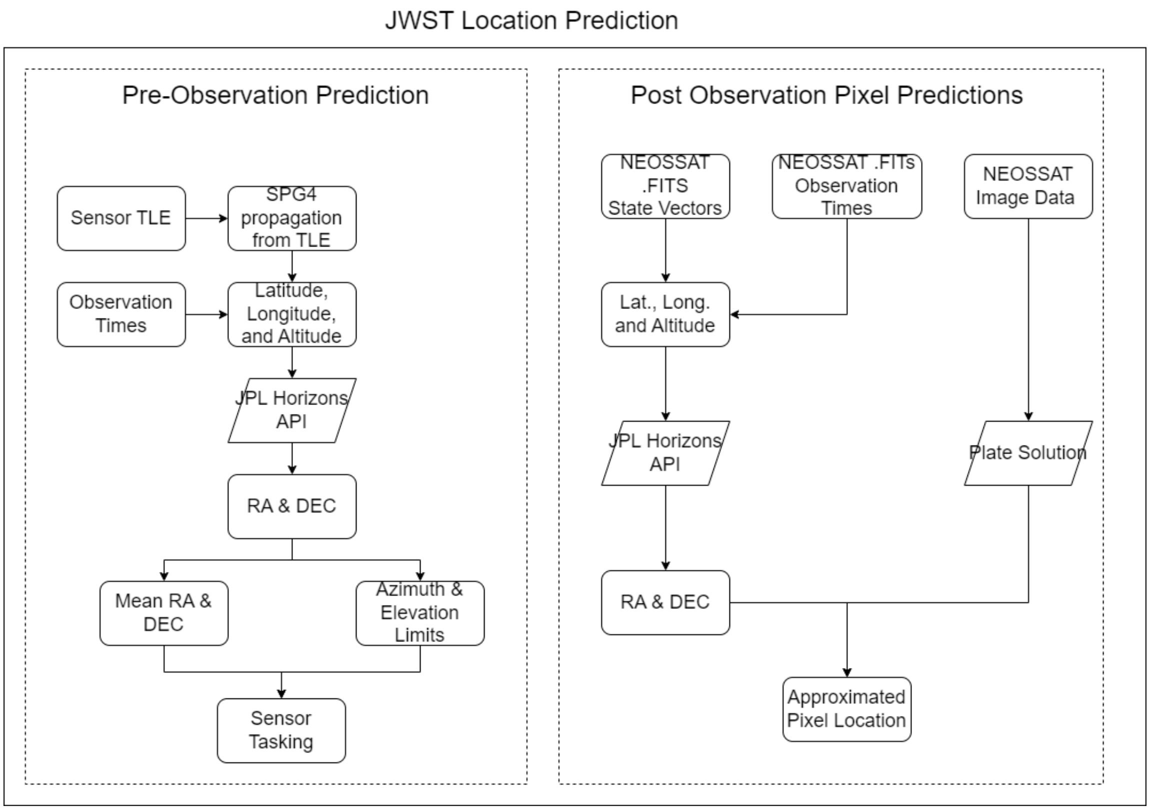

Figure 3.12: JWST location prediction

Initial Prediction

For the chosen date of March 08 2023, the up-to-date epoch TLE for NEOSSat was obtained from Celestrak.org and defined as an *EarthSatellite* object in a script using *skyfield* [36]. The satellite object was then cast to latitude, longitude and altitude using a WGS84 ellipsoid at the image's times plus half their exposure time. After, the JPL Horizon is queried using the longitudes, latitudes and altitudes of the *EarthSatellite* object at mid-exposure time and the 'topocentric' right ascension and declination of JWST are outputted (refer to Section 2.2.4). A Digitized Sky Survey (DSS) image was generated using AstroPy's *astropan* to cover the extent of the right ascensions and declination generated. The World Coordinate System (WCS) information from the generated image is used to 'draw' the pixel locations of the right ascension and declination creating Figure 3.13. One orbit of NEOSSat is seen on the right image of Figure 3.13 when the epochs are restricted to a 105 minute spread.

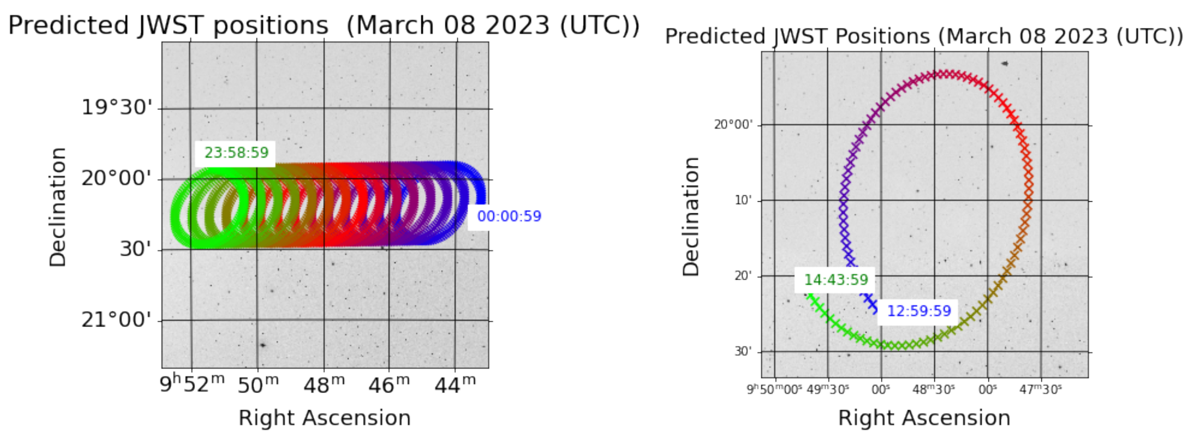

Figure 3.13: Predicted location of JWST with DSS background

The path that JWST takes when viewed from NEOSSat follows an elliptical pattern. The circular shape shifts slightly with each rotation and NEOSSat is adjusted to compensate for every orbit (1 orbit being 105 minutes). NEOSSat was aimed at the middle of the circular pattern for several reasons: image processing would be simplified with star matching and NEOSSat cannot accurately track RSOs with small mean motion (relative to other RSOs). The ideal predicted location presented in Figure 3.13 is not representative of NEOSSat's orbit as the sensor will move behind the Earth, obstructing the view to JWST. In order to model restrictions of NEOSSat's look angles, the satellite is mimicked as a ground-based station. The 'ground-based' 'topocetric horizon' look angles (azimuth and elevation) (See Section 2.2.3) are calculated along with the topocentric right ascension and topocentric declination (See Section 2.2.4) and an elevation restriction of 0 degrees is applied to the prediction location data resulting in Figure 3.14.

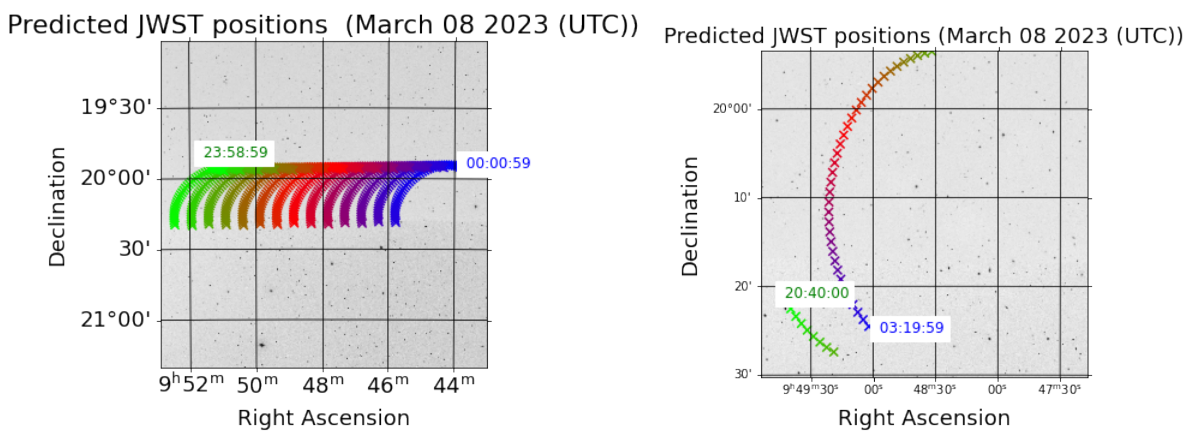

Figure 3.14: Estimated locations of the JWST as seen from NEOSSat with elevation restrictions

3.3 Data Reduction

As previously discussed in section 2.4.3, Bias, Dark and Flat frames can be captured and used to "reduce" raw images to result in higher SNR of the light sources in an image. The IntelSat 10-02 dataset images posses a FOV of 0.79 degrees while the AnikF1 dataset has a FOV of 1.04 and the NEOSSat images of JWST have a FOV of 0.64 degrees.

3.3.1 Bias Frames

With the the image reduction pipeline in mind (figure 3.20) the bias frames were combined in each dataset to create a master bias. The produced master biases are seen in Figure 3.15, which are displayed at their mean values plus and minus 1 standard deviation. Each sensor exhibits a different noise floor and thus will produce a different instrumental magnitude of the same object.

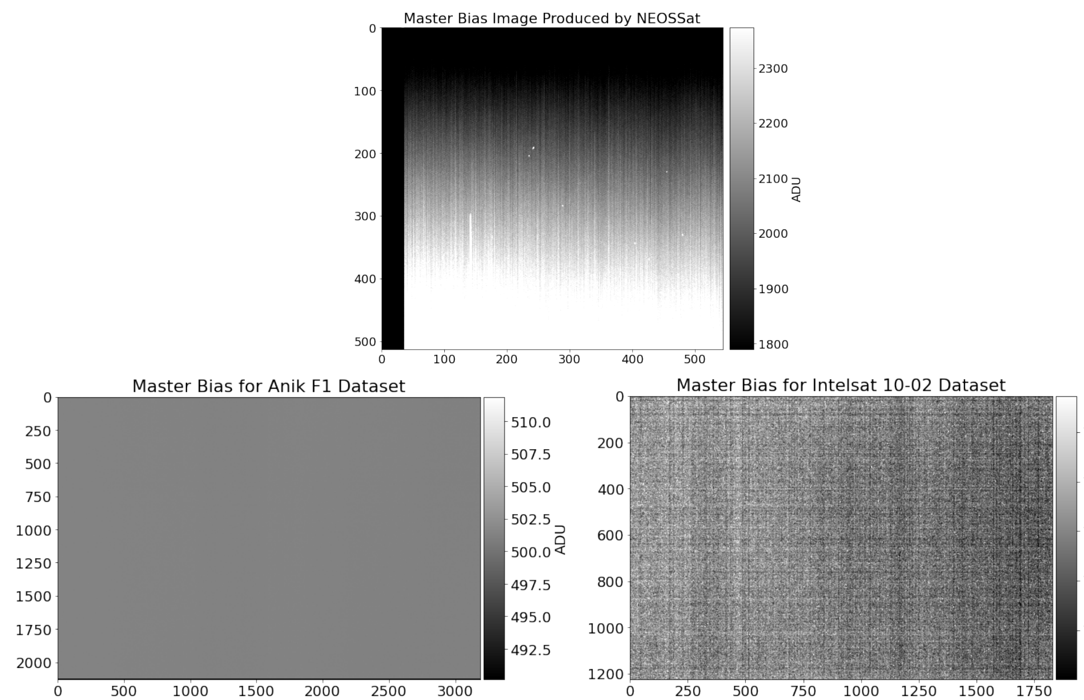

Figure 3.15: Master biases (left to right) from the NEOSSat dataset, Anik F1 dataset and IntelSat 10-02 dataset

3.3.2 Dark Frames

Each dark frame was de-biased (the master bias was subtracted from each frame) and combined according to their filters. The dark frames are displayed in Figure 3.16 at their mean values plus and minus one standard deviation.

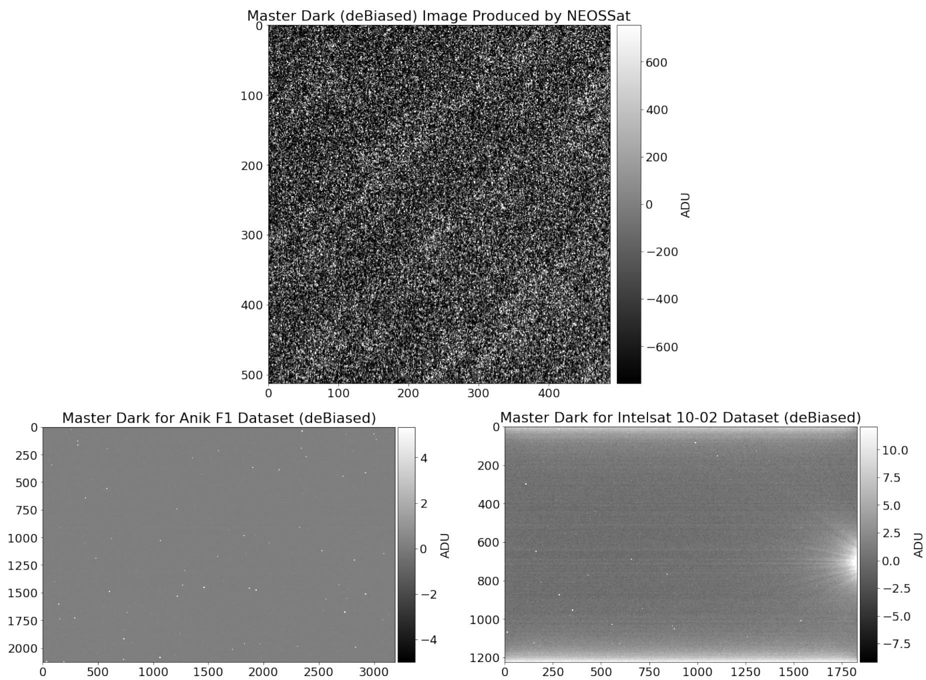

Figure 3.16: Master darks (left to right) from the JWST dataset, Anik F1 dataset, and IntelSat 10-02 dataset

3.3.3 Flat Frames

Although the data reduction pipeline calls for flat frames calibrations, this step could not be completed due to the nature of the NEOSSat sensor and in-accurate captures of flat frames during GBO observations.

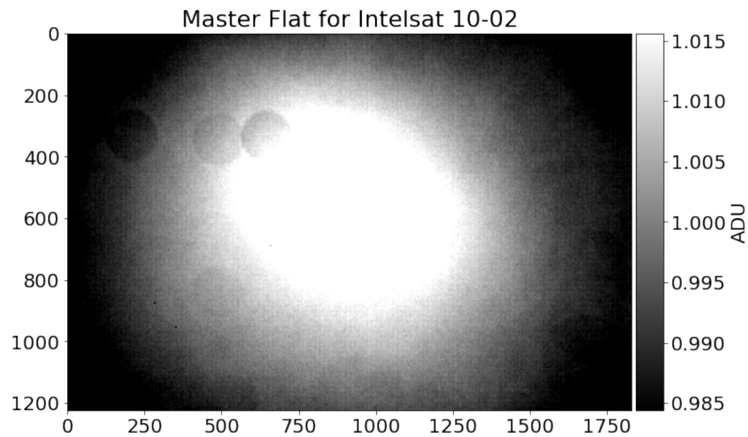

Figure 3.17: Master flat for the IntelSat 10-02 dataset

3.3.4 Additional Processing

NEOSSat's images are additionally processed through a DRDC proprietary software package that performs Fourier analysis on the wave-like structure of the noise floor and subtracts it from the images. The overscan region (region of the left of figure 3.21) of the NEOSSat images is also taken into account to identify additional noise and subtract from the exposed part of the image. The image is then trimmed so that the result only contains the exposed part of the image.

3.3.5 Reduced images

Subtracting the bias and dark frames from the light images a reduced set of images was created seen in Figure 3.18, 3.19 and 3.21.

AnikF1

Figure 3.18 shows the unreduced and reduced images with the Anik F1 dataset.

IntelSat 10-02

Unreduced and reduced images of the IntelSat 10-02 dataset are seen in Figure 3.19.

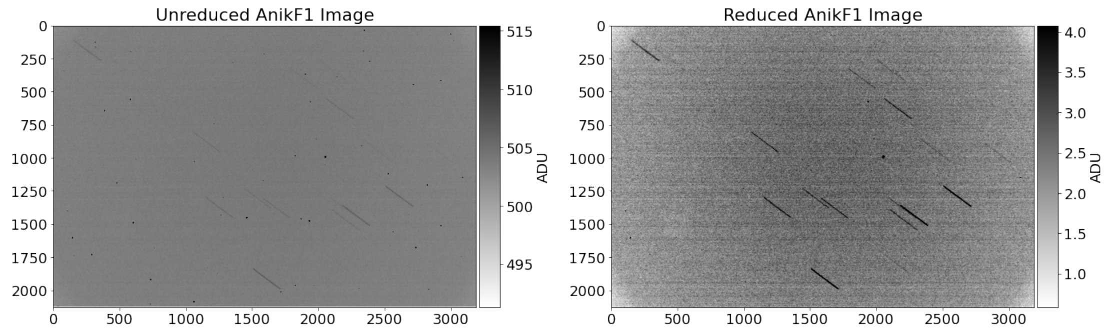

Figure 3.18: Anik F1 unreduced (left) and reduced (right)

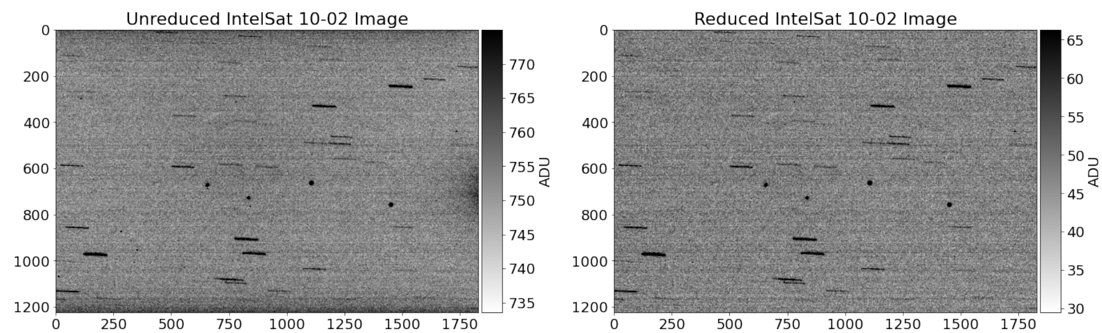

Figure 3.19: IntelSat 10-02 unreduced and reduced

JWST

Due to NEOSSat having poor temperature regulations, images are reduced using a modified pipeline seen in Figure 3.20.

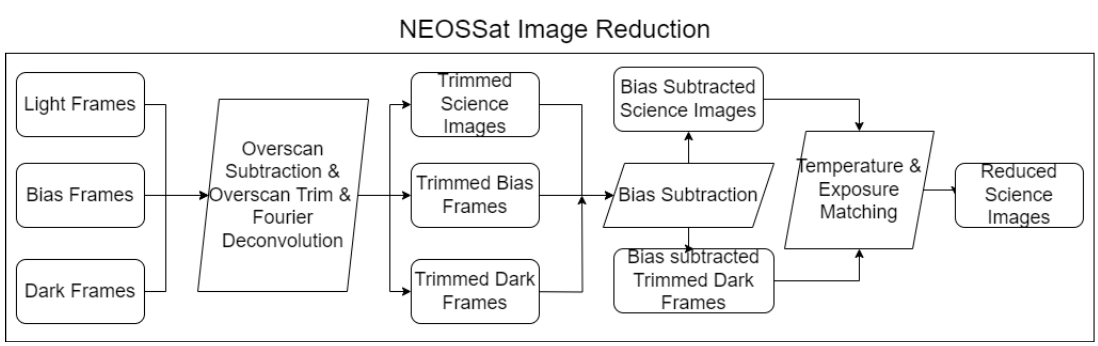

Figure 3.20: Image reduction of NEOSSat images

Using the modified NEOSSat reduction pipeline with deconvolution, a reduced image was produced seen in Figure 3.21.

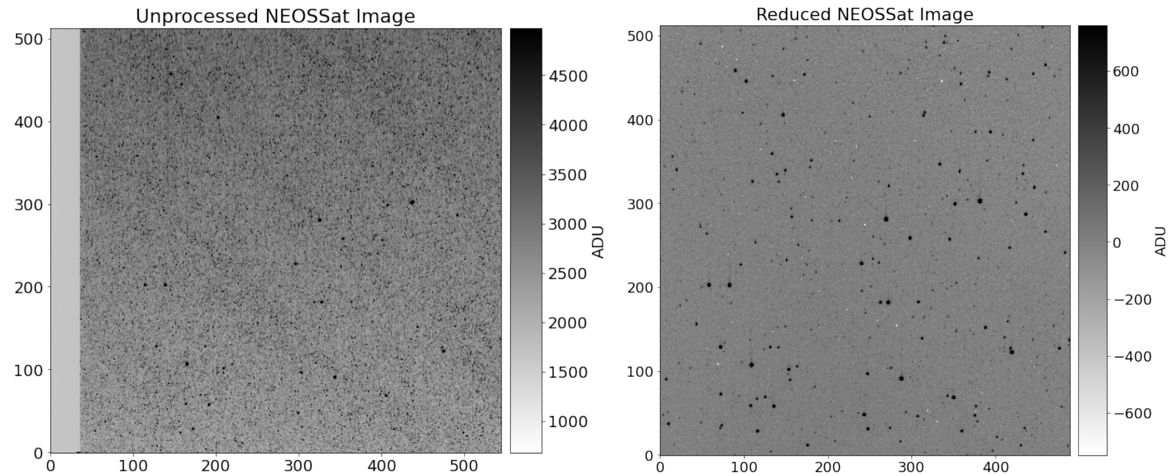

Figure 3.21: NEOSSat unprocessed (left) and reduced image (right)

3.4 Data Acquisition

Figure 3.22 displays the Celestron 8" amateur telescope utilized to capture the AnikF1 dataset. The equipment used included a ZWO ASI 6200MM Pro (Mono) and ZWO LRGB Filters. The Celestron Mount was operated via Skytrack (figure 3.23), while TheSkyX was used to control the filter and data capture rate.

Figure 3.22: Celestron telescope used to capture AnikF1 images

The first dataset was captured in the winter of 2022 and included observations of IntelSat 10-02 and starfield SA 23.

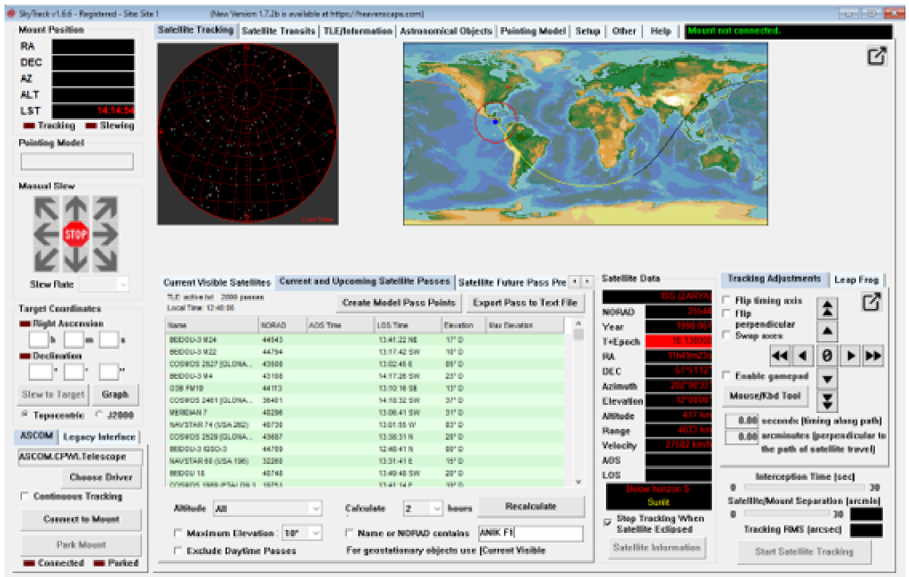

Figure 3.23: Skytrack software used to track RSOs

3.5 Photometry

3.5.1 Background Estimation and Subtraction

The backgrounds were estimated using a Source Extraction and Photometry Package (SEP) algorithm, these estimates were subsequently subtracted from the input science image. Two implementations of the algorithm, SEP and PhotUtils Source Extractor, are shown for comparison in Figure 3.24. The resultant background subtracted images, Figure 3.25, contain significantly less background noise than the original frames.

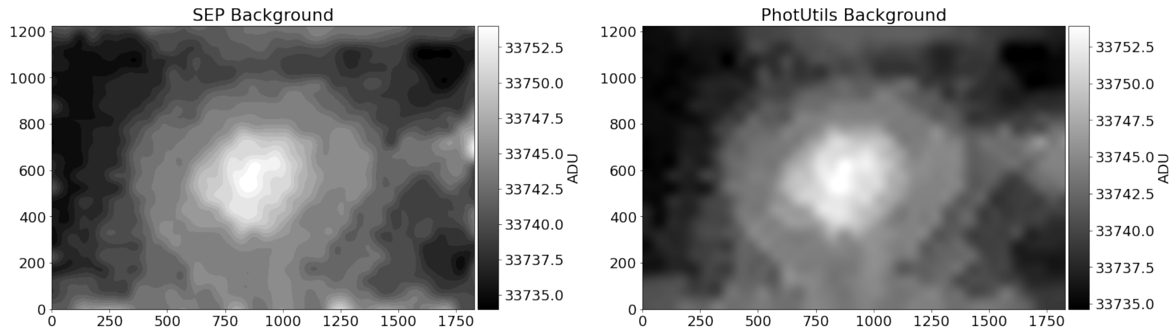

Figure 3.24: Estimated backgrounds

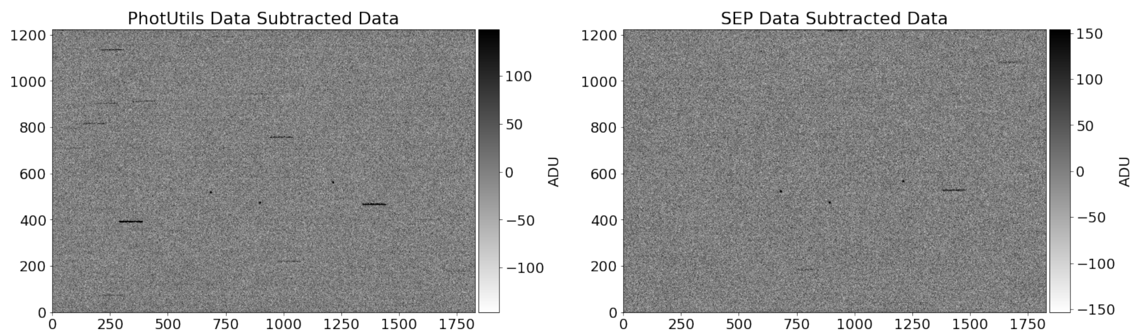

Figure 3.25: Background subtracted images

3.5.2 Source Detection

Track Rate Mode

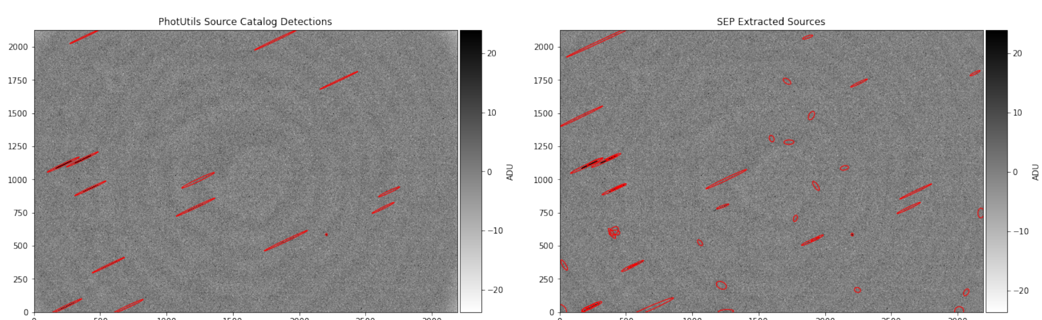

Figure 3.26: AnikF1 Detected with both Photutils and SEP

From analyzing Figure 3.26, PhotUtils is more accurate in detected sources in Track Rate Mode

(TRM).

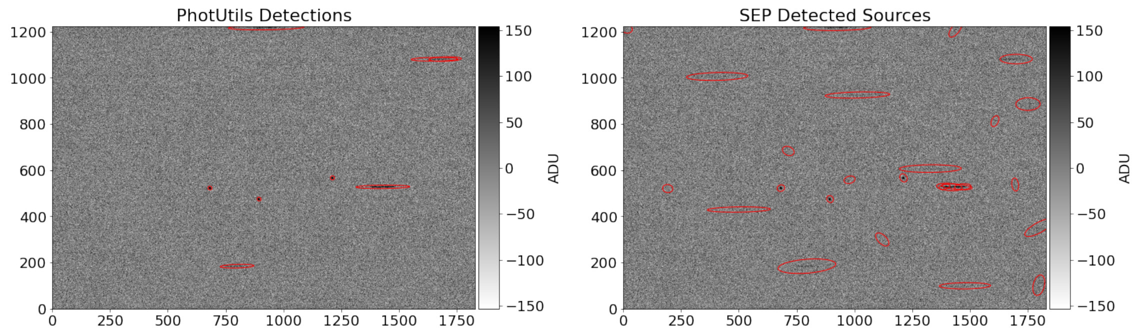

Figure 3.27: PhotUtils (left) and SEP detections (right) with IntelSat 10-02 data

Siderial Stare Mode

For each image in the tested star field dataset, light sources were detected using the three techniques discussed in Section 2.4.4: IRAF DAOPhot, PhotUtils and SEP. Figure 3.28 shows a visual representation of the detected sources as coloured apertures.

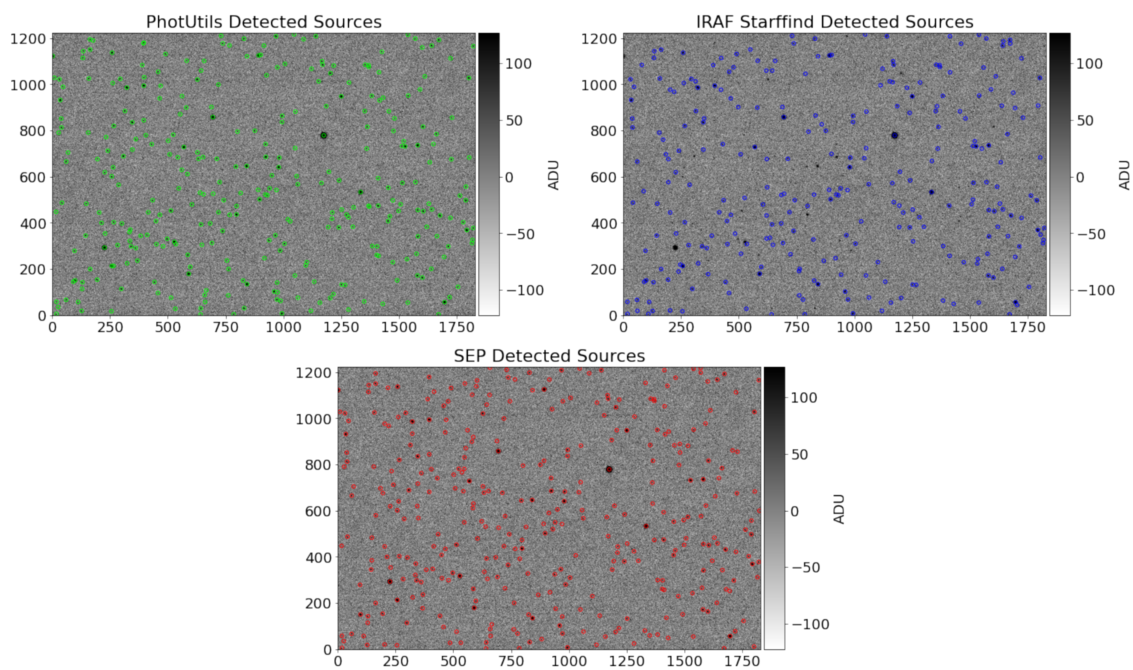

Figure 3.28: Detected stars with different detection algorithms

NEOSSat's data was only detected with the Photutils package due to previous work showing its highest detection accuracy. Figure 3.29 shows an image with the detected NEOSSat sources.

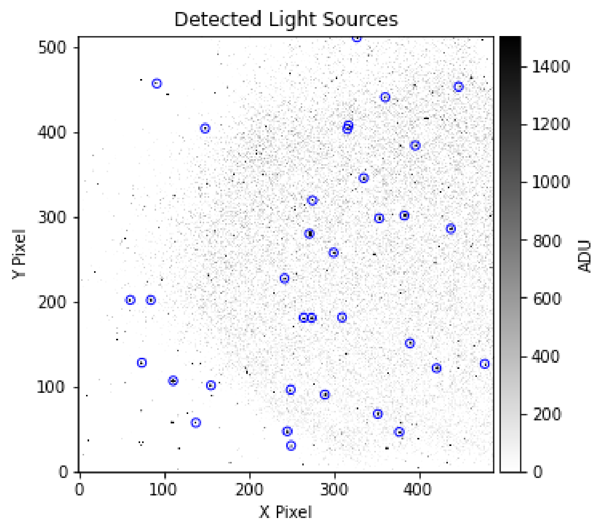

Figure 3.29: Detected sources on JWST imagery with PhotUtils

3.5.3 Source Extraction

Aperture photometry was performed on the light sources by simply placing an ellipse or circle around the light source. A sample image in the dataset was used to determine the required aperture size for aperture photometry.

Optimization

Performing aperture photometry requires choosing an appropriate aperture to measure the light sources in an image. The best aperture was estimated by iteratively measuring the Signal-to-noise ratio (SNR) with different aperture radii.

Signal-to-noise ratio (SNR)

For more accurate measurements, the aperture size was optimized for a dataset by calculating the SNR using Equation 2.34. For each filter in the dataset, the first image had its light sources measured. Figure 3.30 shows how the Signal-to-noise ratio (SNR) varies from star to star in the first blue filter image. Calculating the SNR with Equation 2.34 for all light sources with a range of apertures in an image produced an array of SNR values for each star. Averaging these SNR values across the aperture range gave the average SNR of the light sources in the image for an aperture size. The radius that maximized the average SNR was then chosen as the most appropriate aperture for performing aperture photometry. Table 3.1 displays the optimal aperture radius for the tested images.

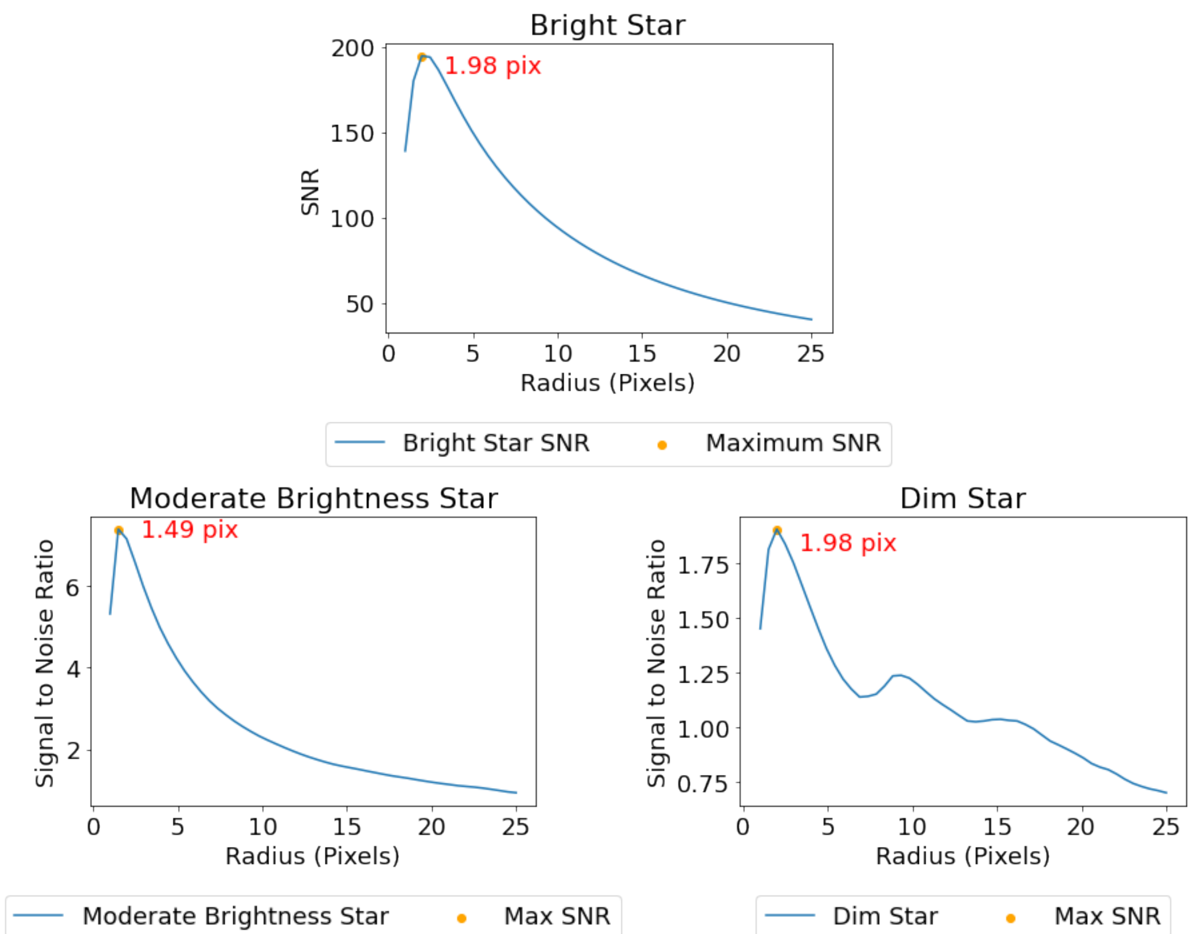

Figure 3.30: Varying SNR of different brightness stars using DRDC's GBO telescope for IntelSat 10-02 absolute photometry

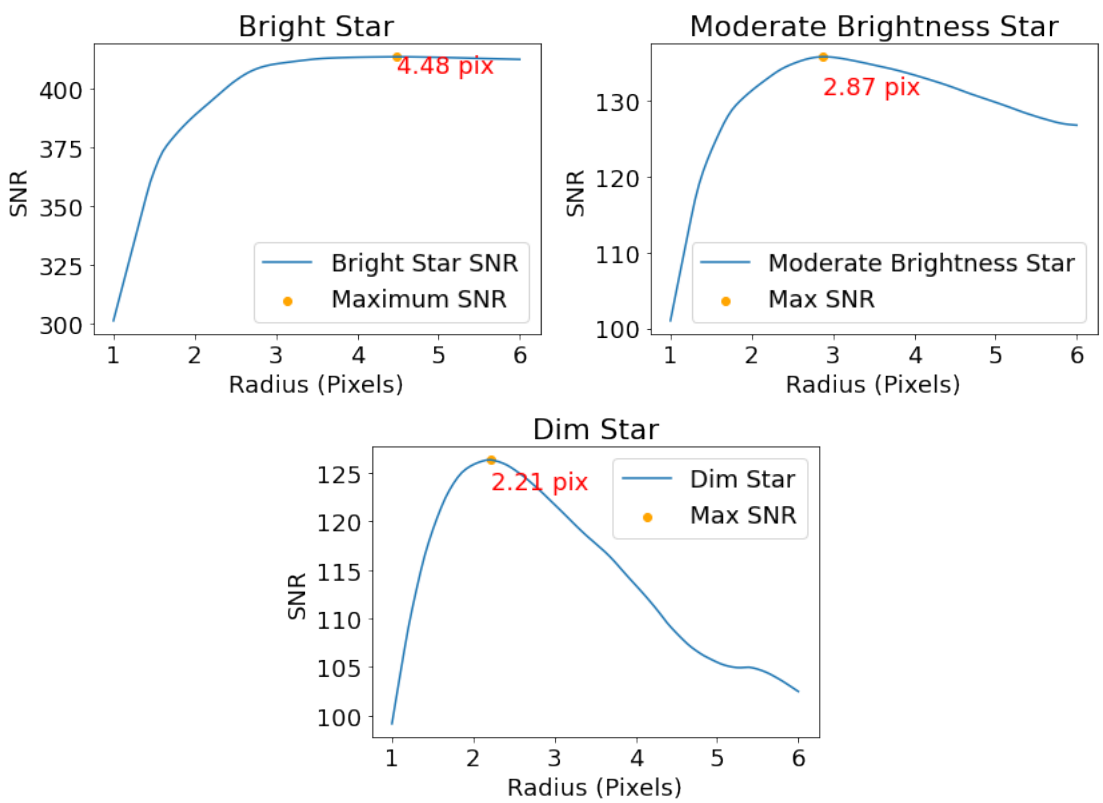

Figure 3.31: SNR of JWST images

Aperture Correction

Using the first image for each filter of a dataset, curves of growth and subsequent aperture correction values were calculated as seen in Figure 3.32 and Figure 3.33 for JWST. The optimal aperture radius and aperture correction values for those radii are seen in Table 3.1.

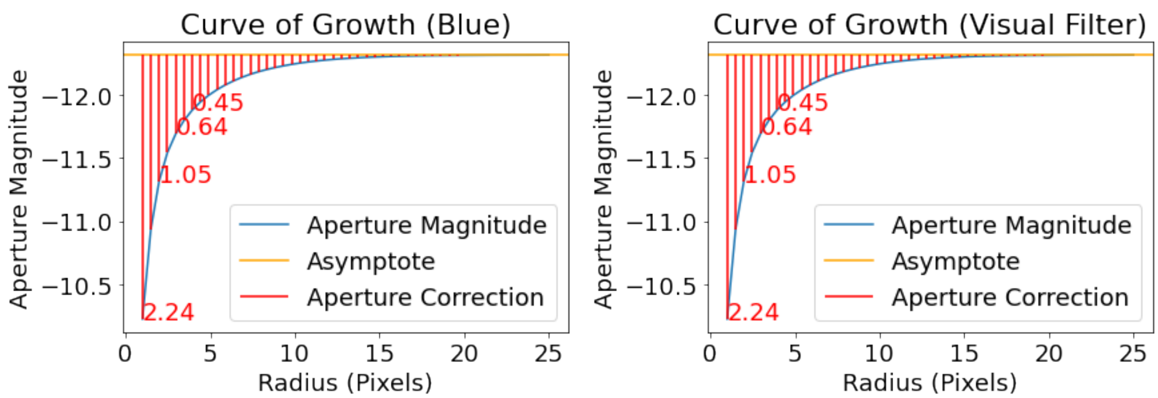

Figure 3.32: Curve of growth analysis with aperture correction values

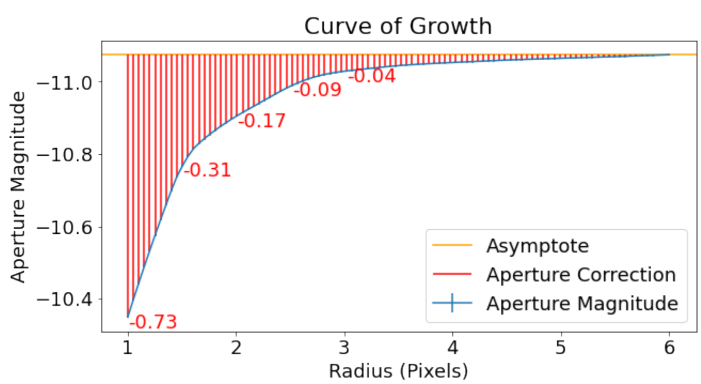

Figure 3.33: Aperture corrections for NEOSSat sensor of JWST images

After the aperture correction values and optimal aperture radius had been found, aperture photometry with a specific aperture, and aperture correction was performed on the images with Equation 2.35 and 2.36.

Filter	Optimal Aperture Radius	Aperture Correction
Visual (Green)	1.97959 pix	1.04963 mag
Blue	1.97959 pix	1.04959 mag
NEOSsat	5.14141 pix	0.01361 mag

Table 3.1: Optimal apertures and aperture correction values

Plate Solving

Plate Solutions were found with *astroquery* package calling nova.astrometry.net service to perform plate solving in the integrated development environment. Each image was tried for a plate solution and WCS information was saved to the FITS image header. Figure 3.34 is a sample image that has been plate solved, and a simulated image with the resolved WCS information on the left shows that the plate solution is correct.

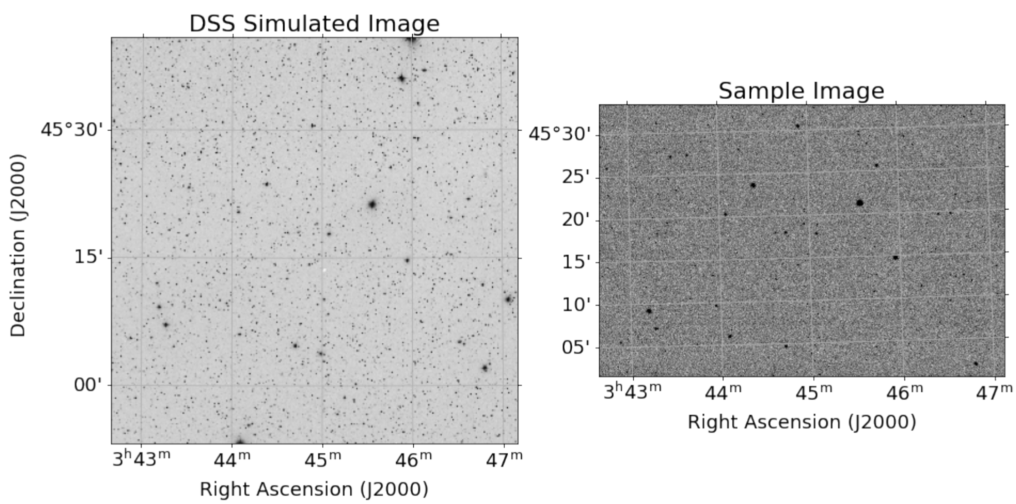

Figure 3.34: Digitized Sky Survey (DSS) simulated image (left) compared to sample image (right)

The images used for observations of IntelSat 10-02 was unable to be plate solved due to it's location in the celestial sphere during observations (see Figure 3.8). For this reason, images of the starfield SA 23 were measured

Catalogue Cross-Matching

Using the right ascension and declination obtained from the plate solution and the image's field of view, the APASS catalogue was sampled with the Vizier service. The imaged stars were then correlated to their respective catalogue stars, within the sample, using the image's WCS information with a distance criteria of 3 arcseconds. The Johnson-Cousins visual and blue standard magnitudes were used for comparison to the blue and green filters used in the AnikF1 and IntelSat 10-02 dataset. From these catalogued values the photometric coefficients were derived (Equation 2.38, Section 2.4.4). The number of star matches and their match accuracy are presented in Table 3.2.

Results	SEP	SourceCatalog	IRAF
Number of Matched Sources	343	312	254
Accuracy Percentage (%)	97.721	97.806	92.36

Table 3.2: Statistics of the matched stars with catalogue stars

3.5.4 Absolute Photometry

The Intelsat 10-02 dataset required the use of absolute photometry due to its lack of catalogue stars in the background of the images.

Transform Coefficients

Iterating over the SA 23 star field images, the absolute photometry transform coefficients were attained by performing the mentioned linear least squares fit. Each source extraction method produced slight variations in their fits, resulting in differences seen in Table 3.3, Table 3.4, and Table 3.5.

SourceCatalog Transform Coefficients

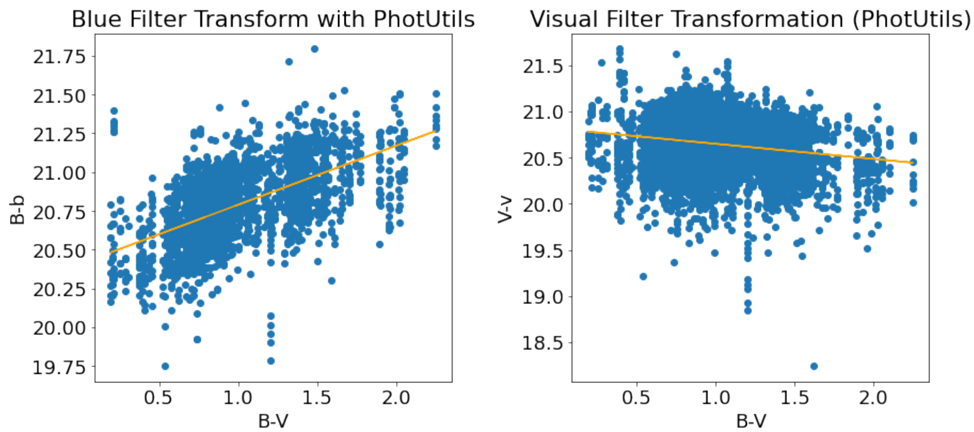

Figure 3.35: Linear least squares fit to find transform coefficients with SourceCatalog extracted stars

Result	Blue Filter	Visual Filter
Transform Coeff	0.31031	-0.11929
Standard Error	0.00991	0.01151

Table 3.3: Transform coefficients from SourceCatalog method

IRAF Starffind

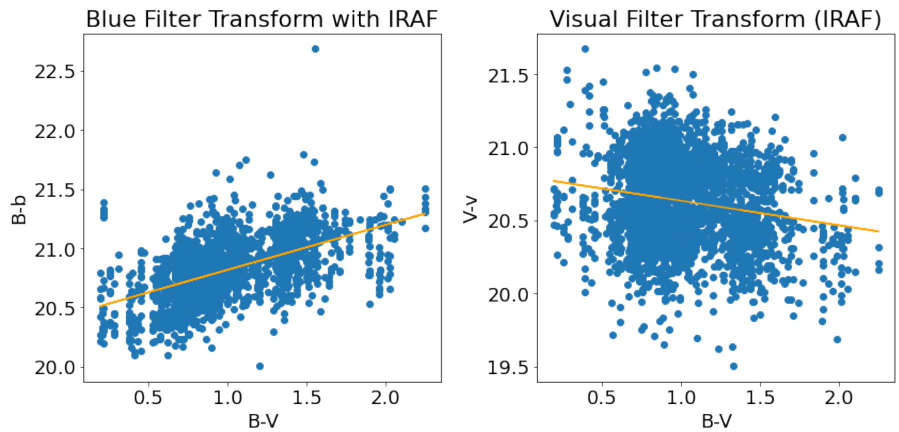

Figure 3.36: Linear least squares fit to find transform coefficients with IRAF Starffind extracted stars

Result	Blue Filter	Visual Filter
Transform Coeff	0.34101	-0.16864
Standard Error	0.01262	0.01554

Table 3.4: Transform coefficients from IRAF Starffind method

Source Extraction and Photometry Package (SEP)

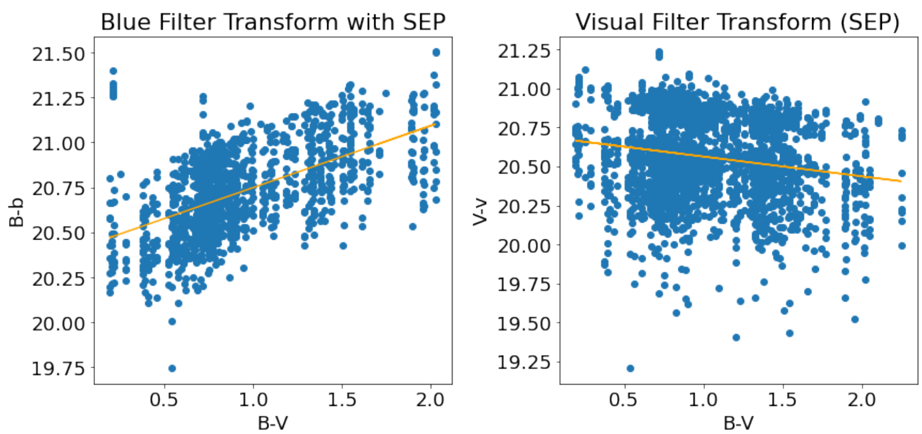

Figure 3.37: Linear least squares fit to find transform coefficients with SEP extracted stars

Result	Blue Filter	Visual Filter
Transform Coeff	0.31353	-0.12457
Standard Error	0.01236	0.01191

Table 3.5: Transform coefficients from SEP method

Extinction Coefficients

Each source extraction algorithm was tried on the SA 23 star field images. The slopes and intercepts of the linear least squares fits became the results seen in Table 3.6, Table 3.7, and Table 3.5.

SourceCatalog

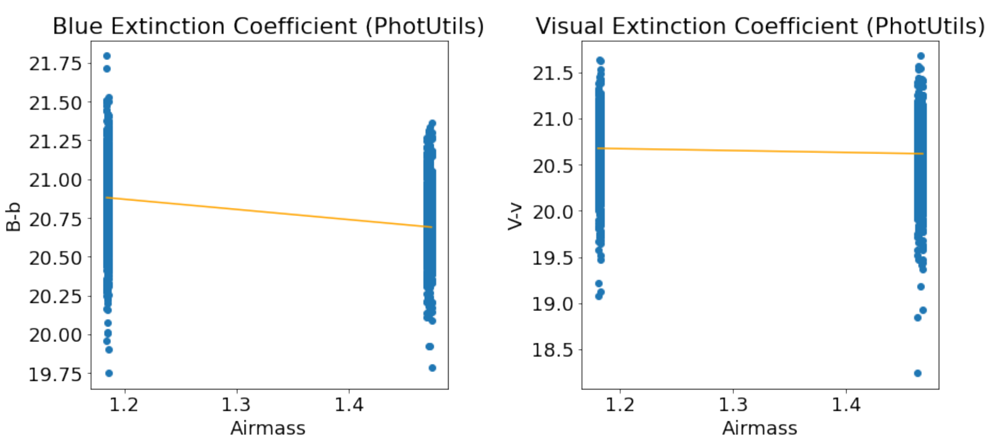

Figure 3.38: Linear least squares fit of the PhotUtils extracted sources to find the transform coefficients

Results	Blue Filter	Visual Filter
Extinction Coeff	0.55484	0.25279
Standard Error	0.03113	0.02418
Zeropoint	21.46023	20.81745
ZP Error	0.004159	0.03215

Table 3.6: Extinction coefficients found from SourceCatalog

IRAF Starffind

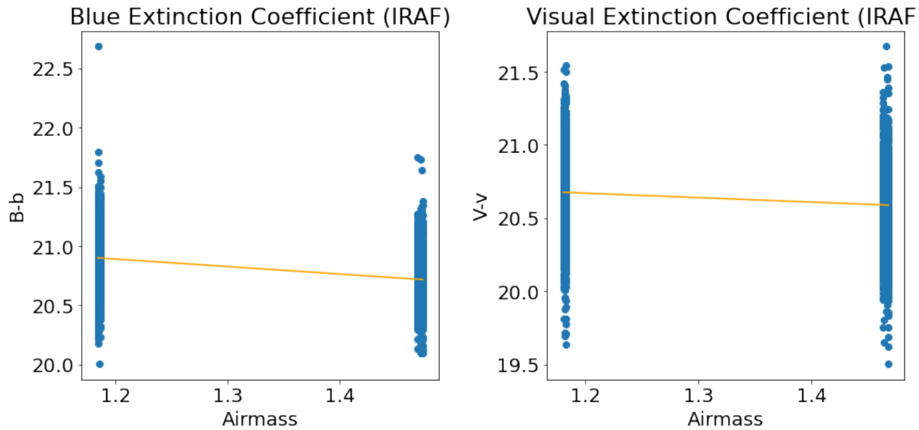

Figure 3.39: Linear least squares fit of IRAF Sources to find the transform coefficients

Result	Blue Filter	Visual Filter
Extinction Coeff	0.52519	0.35030
Standard Error	0.03787	0.03542
Zeropoint	21.42890	20.91822
Zp Error	0.05036	0.04713

Table 3.7: Extinction coefficients found from IRAF sources

Source Extraction and Photometry Package (SEP)

Result	Blue Filter	Visual Filter
Extinction Coeff	0.50866	0.31629
Standard Error	0.04109	0.03772
Zeropoint	21.35310	20.81804
Zp Error	0.05506	0.04344

Table 3.8: Extinction coefficients found from SEP

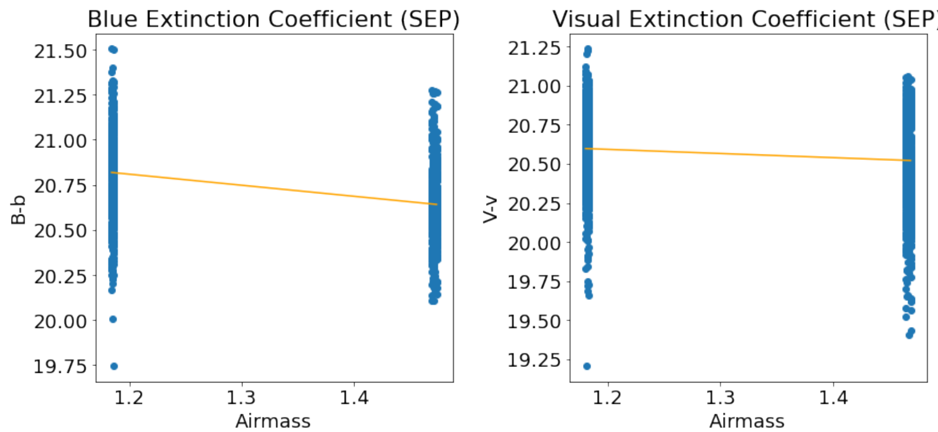

Figure 3.40: Linear least squares fit of SEP detected sources to find the transform coefficients

Colour Index

The approximate colour index (B-V) using Equation 2.39 was calculated for each source extraction method resulting in Figure 3.41 and Table 3.9.

Result	SourceCatalog	IRAF Starffind	SEP
Slope	1.35531	0.87654	1.26905
Error	0.05118	0.04811	0.06159

Table 3.9: Colour index of the extracted sources

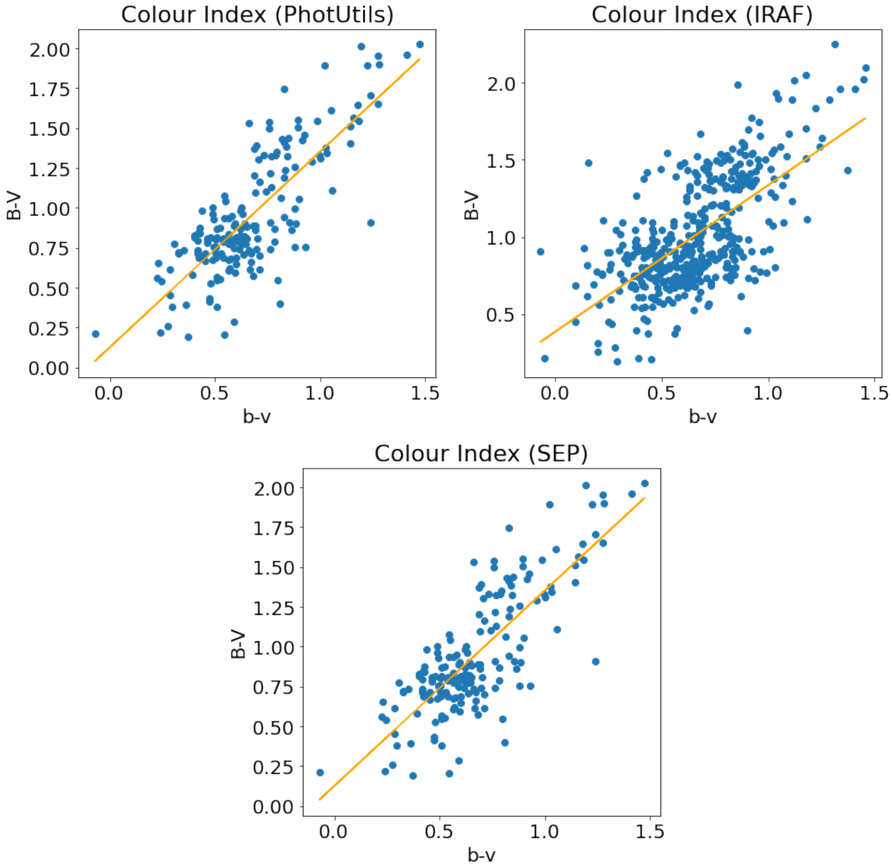

Figure 3.41: Colour index of the extracted sources

3.5.5 Differential Photometry

For the AnikF1 dataset differential photometry was used. Similarly to performing absolute photometry, the colour transfromations were calcualted as seen in Figure 3.42 and Table 3.10 .

	Result	**Error**
Blue Transform	0.17769	0.12926
Visual Transform	-0.10046	0.122

Table 3.10: Colour Transforms from background stars

Leveraging Equation 2.40 and 2.41, the apparent magnitude was then derived from the instrumental magnitude of the RSO.

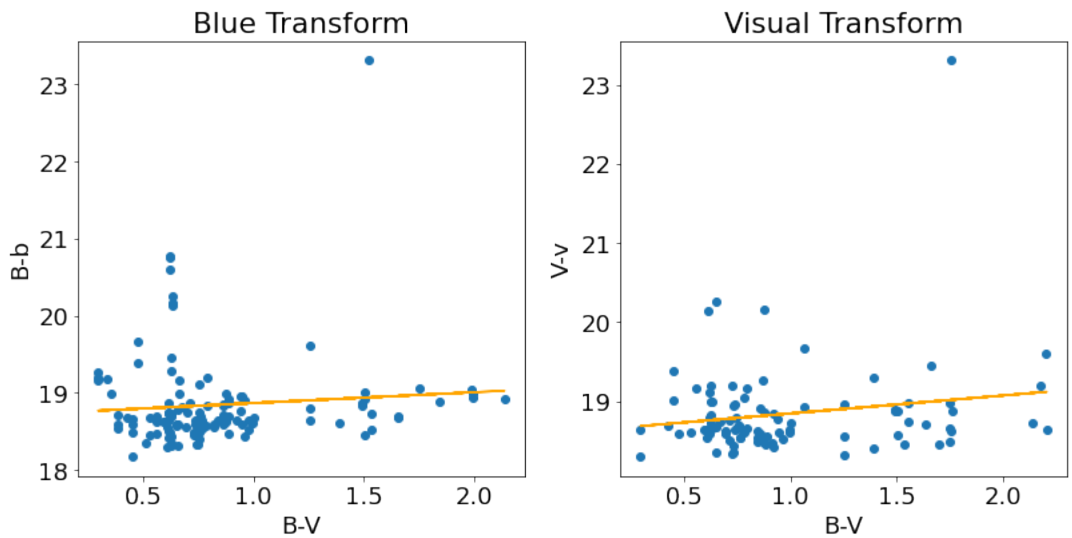

Figure 3.42: Blue and Visual Colour Transformations

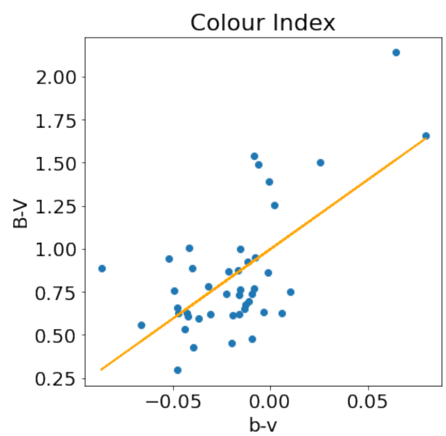

Figure 3.43: Colour index from differential photometry

	Result	**Error**
Colour index	11.84204	1.98648

Table 3.11: Colour Index from AnikF1 Data

3.5.6 RSO Correlation

GEO Track Rate Mode Photometry

When identifying RSOs in TRM, the shape of the detected sources were used to isolate the RSOs in imagery. Since RSOs were being tracked they would appear as circles while the stars would appear

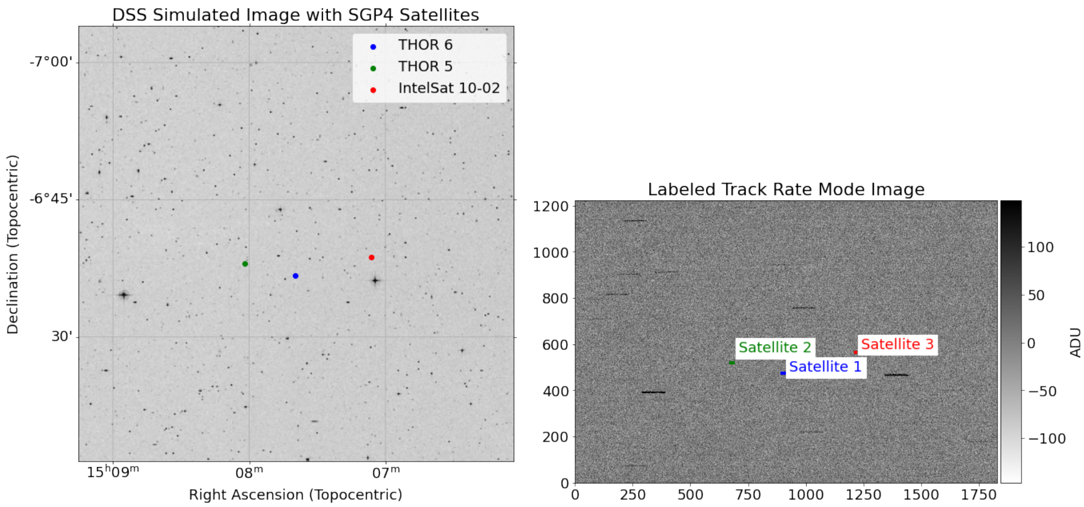

Figure 3.44: Simulated View of RSOs near Intelsat 10-02 with satellites seem in the image

as streaks leading to more oblate detections. To identify the RSOs when multiple are present, such as the data obtained of IntelSat 10-02, satellites with similar Right ascension of the Ascending Node are propagated using their TLEs along with the target satellite and plotted on a simulated image. Figure 3.44 shows a generated image of IntelSat 10-02, Thor 6 and Thor 5 plotted next to a captured image.

JWST

For imagery captured of JWST in Sidereal Stare Mode (SSM) by NEOSSat, the target RSO also appeared as a point source. Using the prediction location in Section 3.2, a cutout of the image is created. Sources are detected within the cutout and the closest source to the predicted location was tagged as the target RSO. The simple proximity method chosen will tag the wrong light source when conjunction occurs, requiring filtering after calculating the light curve of the RSO and it's residuals. The predicted locations of JWST were used to direct the sensor and capture a series of 100 images per orbit for several orbits. The images captured contained accurate values for cartesian state vectors and the latitude and longitude of NEOSSat saved in the image's .FITS headers. The state vector was used to predict the height above the WGS84 ellipsoid which was then used jointly with the measurements of latitude and longitude as inputs for JPL Horizon's API. On March 08th 2023, the following predicted locations were produced in Figure 3.45.

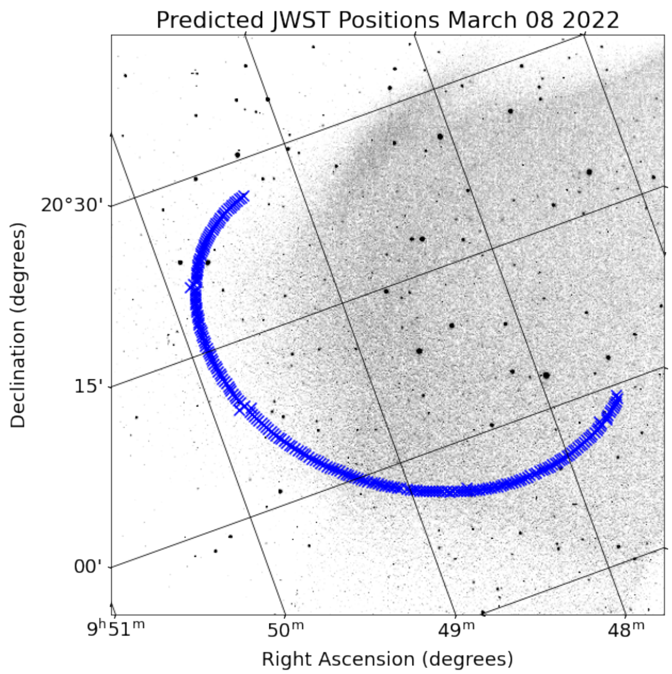

Figure 3.45: Predicted locations of JWST displayed on a background star field on March 08 2023

Chapter 4

Results

4.1 Intelsat 10-02 Photometry

Applying the absolute photometry equation (Equation 2.38) to the instrumental magnitudes, the apparent magnitude was approximated. Calculating the apparent magnitudes for the IntelSat 10-02 images with different extraction methods used to find the photometric coefficients resulted in Figure 4.3 and Figure 4.2 for each filter used.

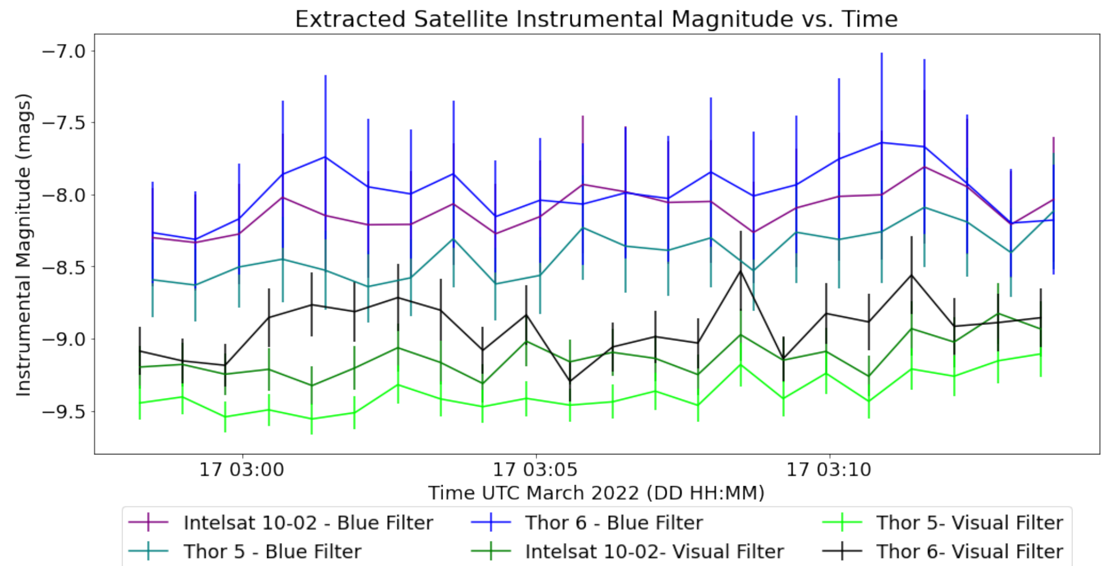

Figure 4.1: Instrumental Magnitude

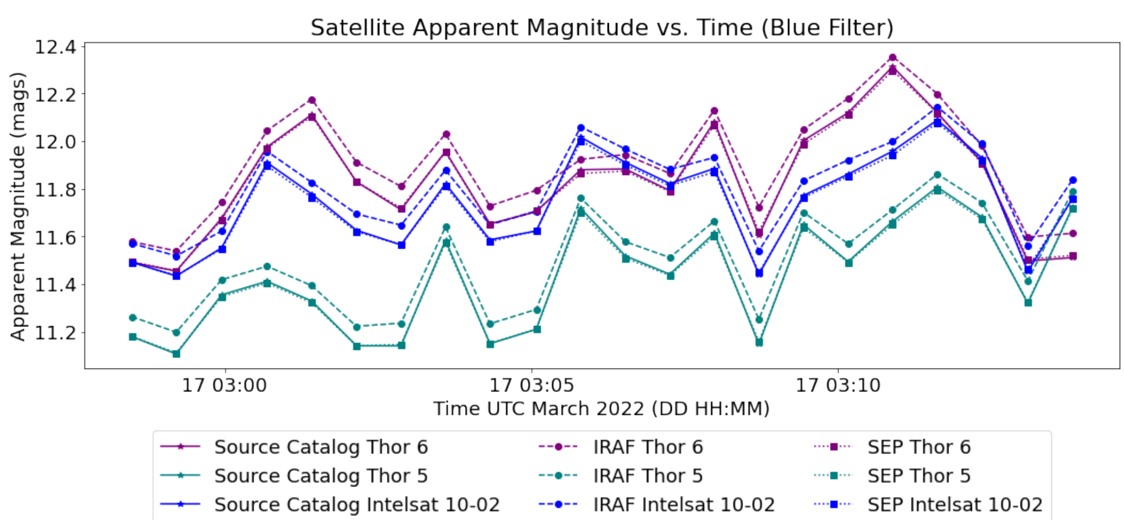

Figure 4.2: Apparent Magnitude in the blue filter with different source extraction methods

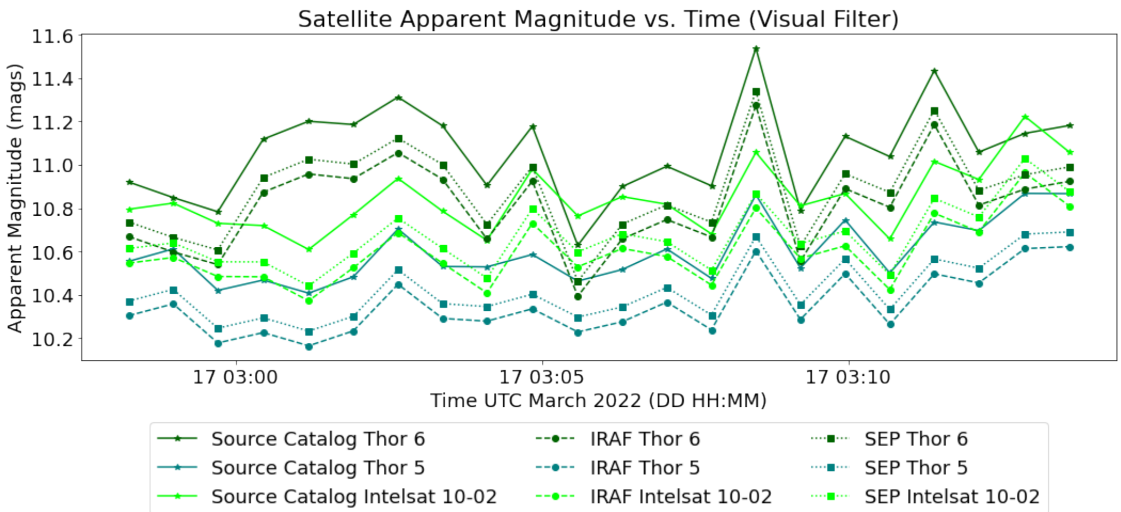

Figure 4.3: Apparent Magnitude in the visual filter with different source extraction methods

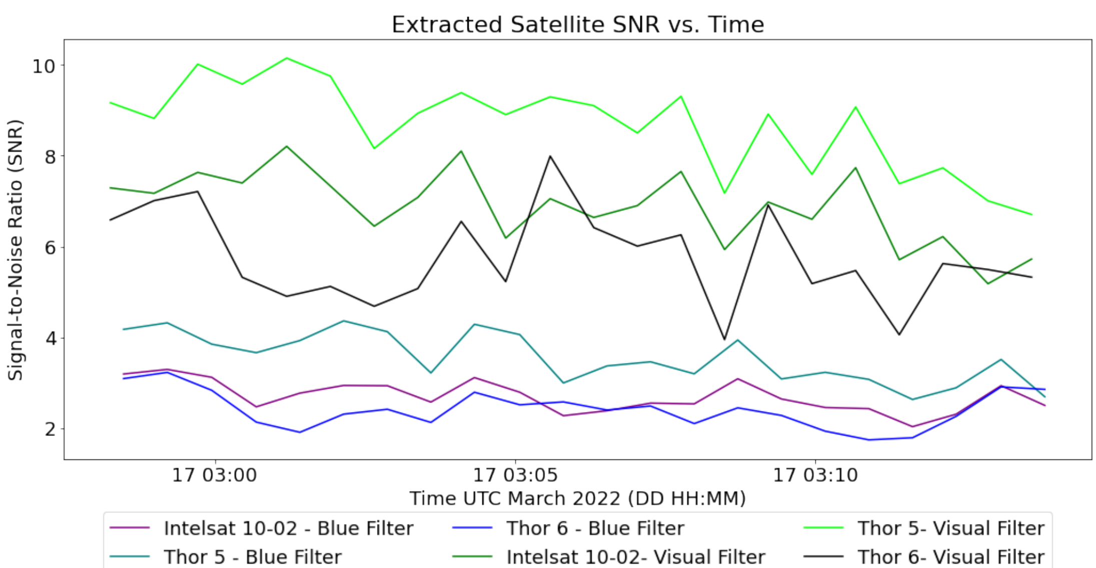

Figure 4.4: SNR of targeted RSOs

4.2 AnikF1 Photometry

AnikF1 was measured with both the ZWO Green and ZWO Blue filter producing Figure 4.5.

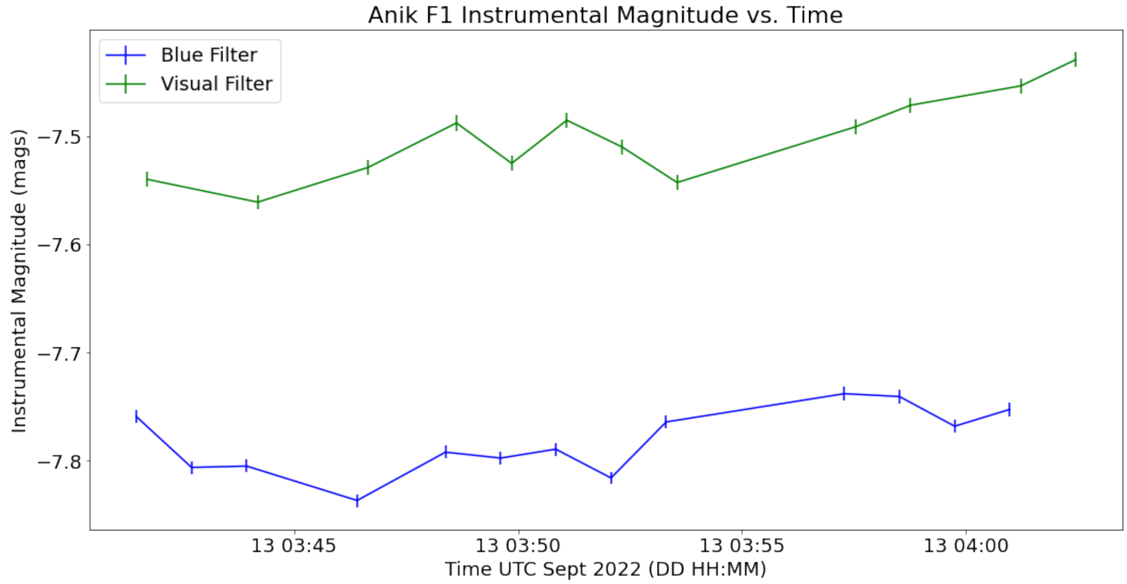

Figure 4.5: AnikF1 instrumental magnitude

Applying the differential photometric methods discussed in Section 3.5.5 to Figure 4.5 produces Figure 4.6.

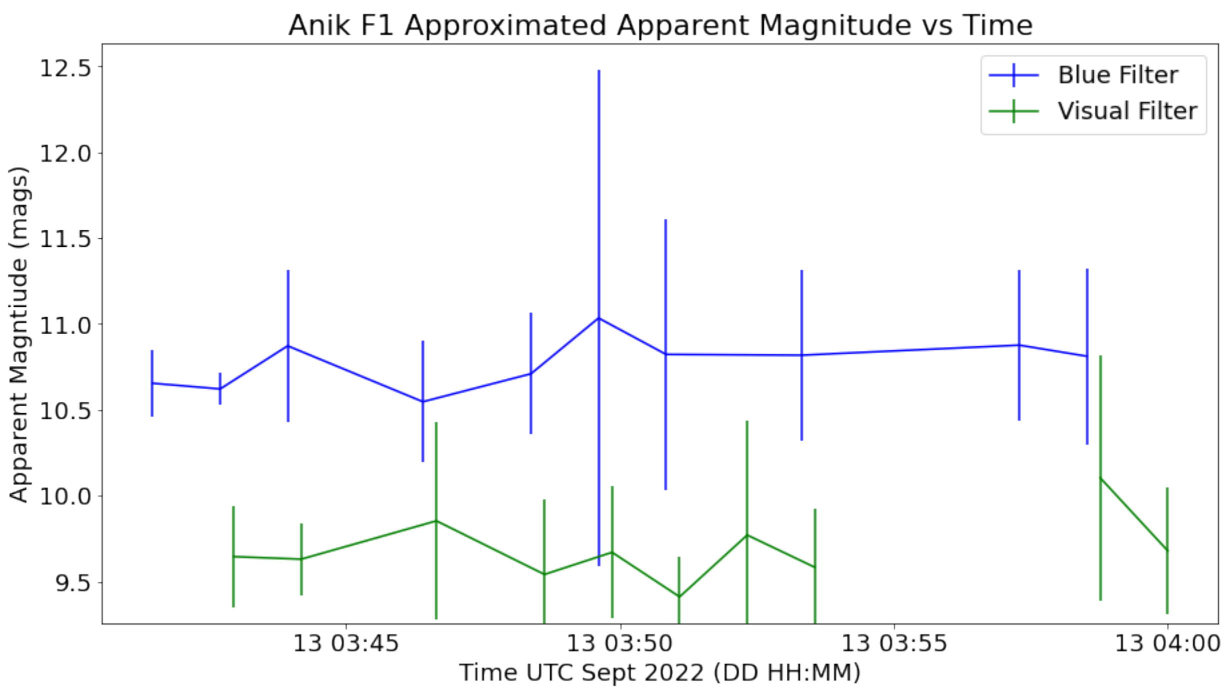

Figure 4.6: Anik F1 apparent magnitudes

4.3 JWST Photometry

With the appropriate aperture radius chosen from Figure 3.30 and Figure 3.31, aperture correction from Figure 3.32 and Figure 3.33, and predicted locations from Figure 3.45 the aperture and instrumental magnitudes of JWST are extracted resulting in Figure 4.7.

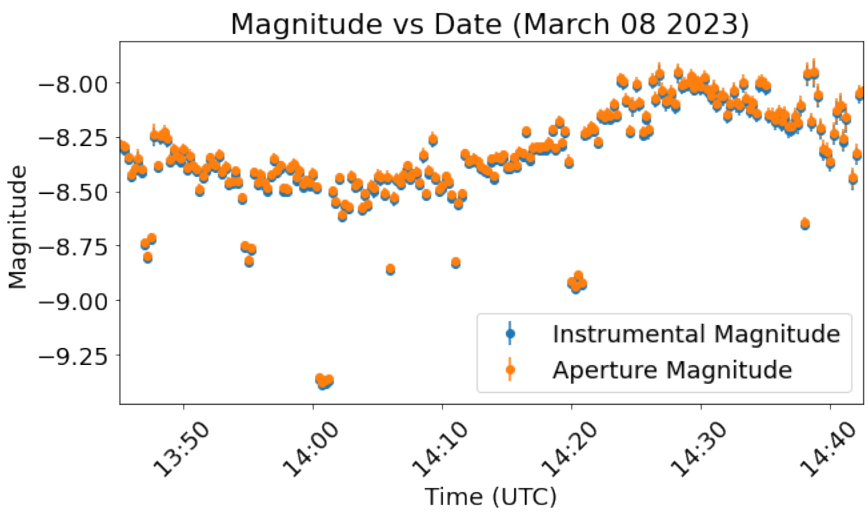

Figure 4.7: Instrumental and Aperture Magnitude

In the background of all the images, stars are detected stars, and with the aperture radius calculated in Figure 3.30 and Figure 3.31, the instrumental magnitude of the brightest 20 stars are extracted. Comparing the detected stars to their catalogue values, results in zeropoint values in Figure 4.8.

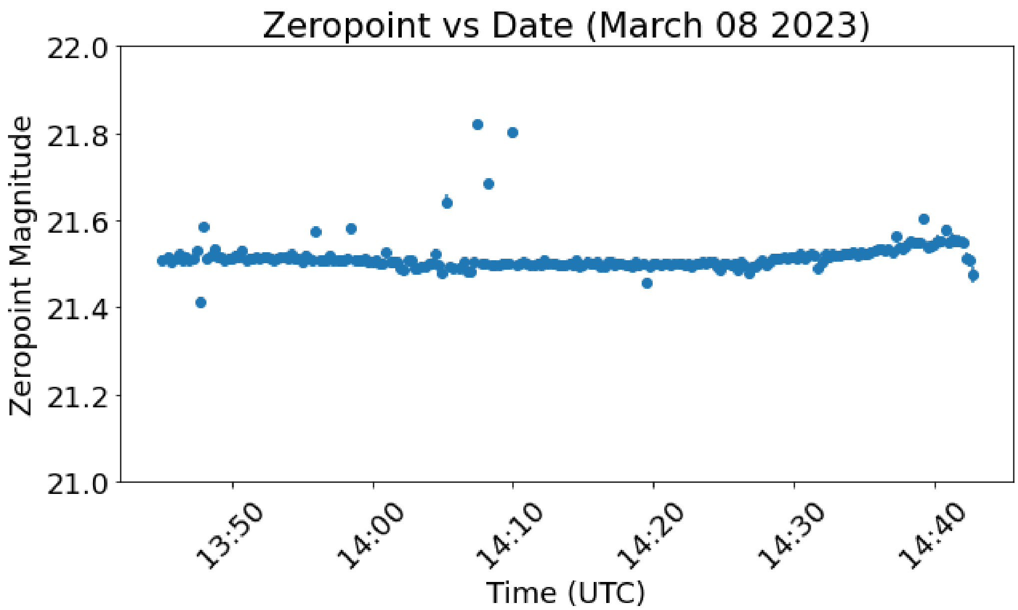

Figure 4.8: Zero points plotted against time

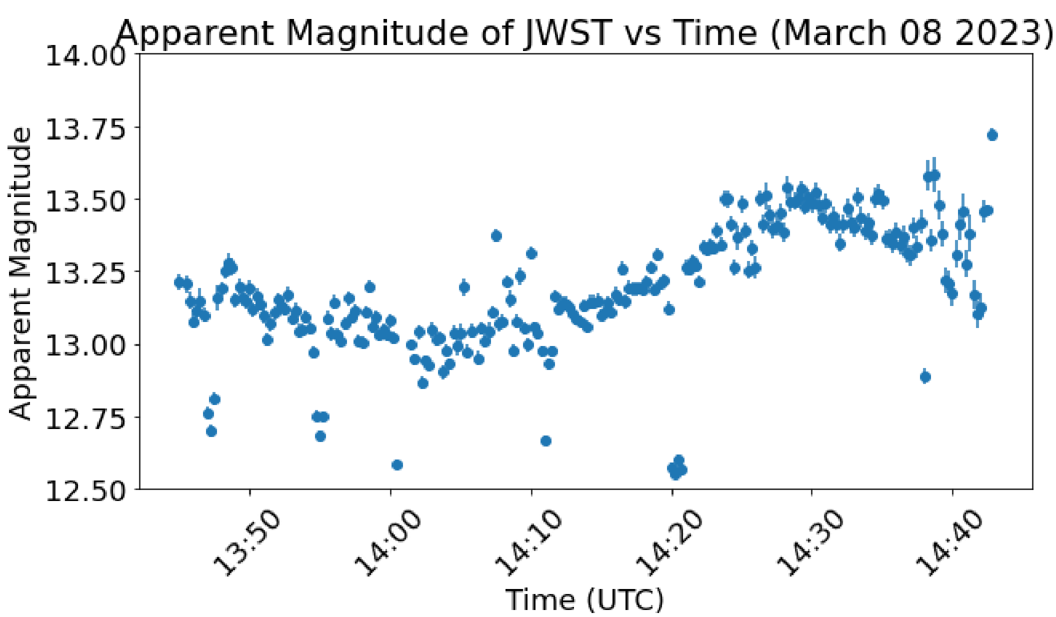

Figure 4.9: Apparent Magnitude vs Time

4.4 Astrometric Measurements

Comparing where the RSOs should be and where they're measured, a measurement of their offsets called residuals can be created. Figure 4.12 displays the residuals of JWST while Figure 4.11 displays the residuals of AnikF1.

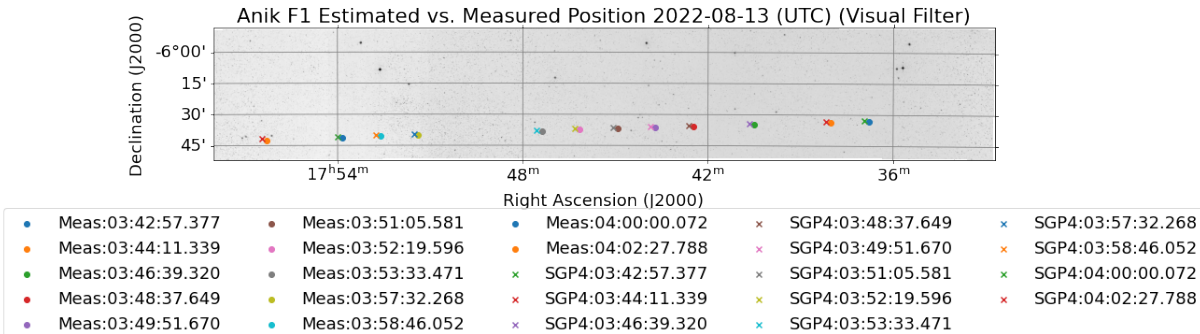

Figure 4.10: Astornmetric Values of AnikF1

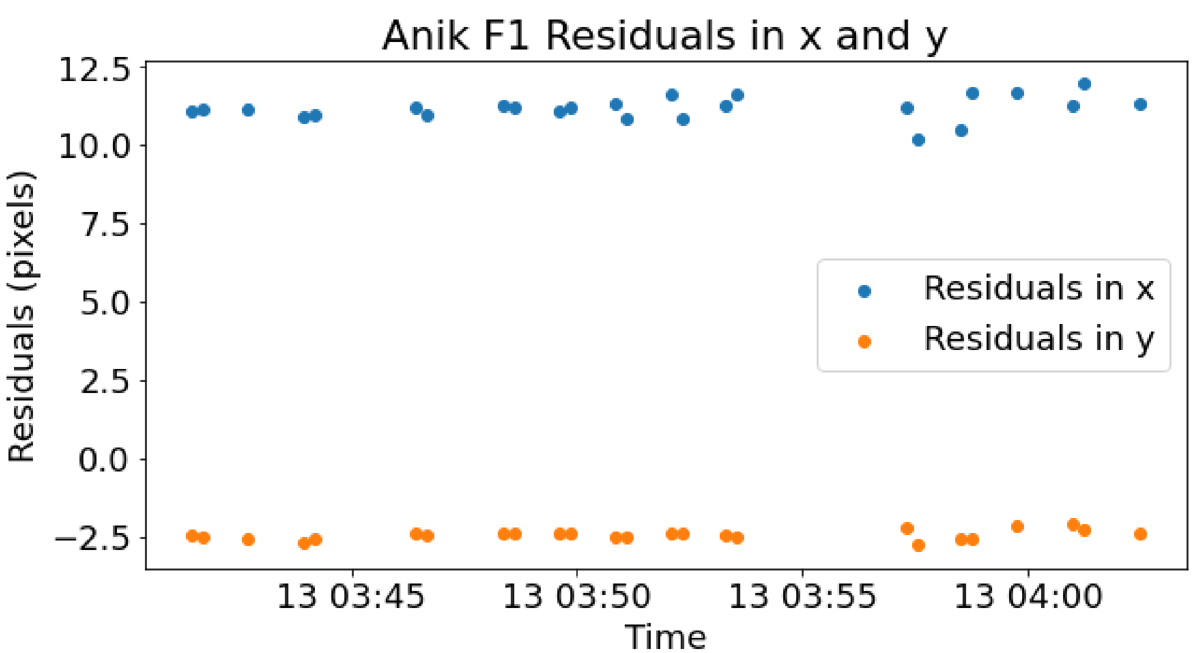

Figure 4.11: Anik F1 Residuals

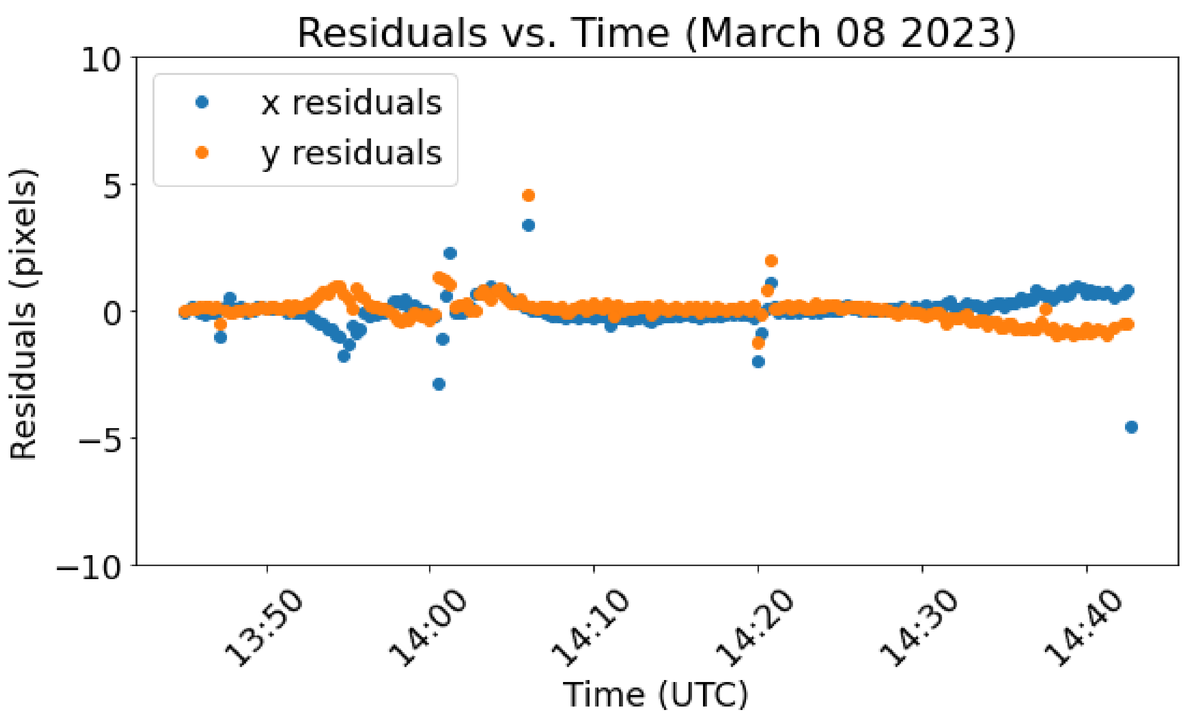

Figure 4.12: Residuals for the JWST Data

4.5 Discussion

4.5.1 Image Reduction

For both ground-based and space-based images the greatest contributor to noise was the sensor noise. While the ground based images had the typical noise features of the astronomy sensor and were able to be reduced with bias, darks and flat frames, the space-based images from NEOSSat showed sinusoidal wave patterns that required a special propriety reduction software to perform Fourier analysis and subtraction. In both types of sensors, the SNR of the light sources were significantly increased, aiding to source detection and extraction.

4.5.2 Astrometry

Ground-based Astrometry

For ground-based data, astrometry was only performed on the AnikF1 dataset due to the greater number of background stars in the images. The difference between the predicted location and the measured locations were around 5 arcseconds, which proved to be a good estimate of position. This difference could be the result of SGP4 propagation errors, stellar aberration, or a number of human errors.

Space-based Astrometry

The process for identifying JWST in images captured by NEOSSat proved to be effective with residuals landing within 5 pixels or 3 arcseconds. Using a simple proximity correlation to the estimated positions, JWST was identified accurately around 97% of the time. Conjunctions with stars in the images created rapid spikes or dips in light, which can then be filtered out in post-processing when analyzing either Figure 4.12 or Figure 4.9. Caution will need to be taken for each processed image dataset to ensure the residuals do not drift drastically.

4.5.3 Photometry

Instrumental Magnitude

The instrumental magnitude light curves exhibited a varying amount of error that was inversely proportional to the SNR (See Equation 2.37) of the measured RSO and relatively low deviation between sequential observations. The lack of deviation is indicative of good seeing conditions.

Absolute Ground-Based Photometry

Common patterns exist when using all three source extraction methods for absolute photometry despite their deviation in zeropoint values. The different source extraction methods showed slight variations due to the nature of the internal algorithms: SEP uses algorithms catered towards galaxy surveys while IRAF relies on a pre-existing PSF kernel for star identification, and *detect_ sources* is a general purpose object detection algorithm built in Python. PhotUtil's detect_ sources with SourceCatalog option proves to be superior in detection accuracy and versatility (offering both deblending and convolution out of the box) and its exclusive use is recommended in further research. Many assumption were made in the absolute photometry equations that could result in error. For one, it was assumed that the second order extinction was negligible for both filters, thus altering the blue filter transformation and blue filter extinction coefficient calculations. The resulting values will change slightly after a second order extinction coefficient is factored into the equations by approximately +/- 0.1 for the extinction coefficient and +/- 0.3 for the colour transformation [21]. It was also assumed that the colour filters used in capturing the images were close enough to the UBVRI values in the APASS catalogue. This fallacy places additional unknown errors on the extinction coefficient and transformation coefficients. The recorded airmass of IntelSat 10-02 was around 3.5518 (Figure 3.7), which could possibly cause some issues with the accuracy of the produced light curve as the extinction coefficient were only calculated using data between 1.48 and 1.1 airmasses. One way to increase the accuracy of the transformation equations is to increase the airmass range and to avoid observing RSOs below 30 degrees elevation. The produced absolute photometry light curves have a combined error from the light source plus the transformations coefficient errors. Although the errors aren't displayed in Figure 4.3 and Figure 4.2, the errors aren't significantly more than the instrumental magnitude errors. It can then be assumed that the largest contributor to the error in the resultant lightcurves is the error baked into the measured light source.

Differential Ground-Based Photometry

Differential photometry from ground-based sensors with narrow FOV proves to be the least accurate of RSO photometry methods with uncertainty largely dependent on the number of stars observed in the background of the images. Differential photometry for ground-based sensors is only recommended in high star density areas of the sky or higher sensitivity scopes allowing for more catalogue stars to be detected resulting in a reduction in error.

Space-Based Photometry

The produced light curve of JWST, seen in Figure 4.9, shows minimal variations besides the expected sinusoidal wave resulting from the change in distance between JWST and NEOSSat. The lightcurve of JWST has little error due to NEOSSat being able to see more stars above the atmosphere and the slow moving nature of JWST allowing for longer exposure periods. Future space-based measurements should be normalized by distance to reduce this dimming pattern. The pattern seen in the light curve may also be caused by a change in the look angle of NEOSSat as it orbits around the Earth that affects the light measured. Further investigation will need to be conducted on a larger dataset to attempt to associate changes in light curve spikes with changes in the observed targets by JWST.

Chapter 5

Conclusion

A set of Python tools were successfully created to handle ground-based absolute photometry, ground-based differential photometry and space-based photometry. For absolute photometry all three source extraction methods exhibit shared patterns, despite their variance in zero-point values. Ground-based differential photometry proved to have limited use for narrow FOV sensors such as the sensors used (all around 1 degree or less). However, differential photometry is effective in performing photometry with space-based sensors on distant objects. All methods that were tried produced light curves of varying accuracy with some exhibiting unidentified sinusoidal patterns. Further development and application of the software package are recommended to build upon the foundations laid out in this research.

5.1 Contributions

With the growing concern over SSA and the limited literature on RSO photometry, this thesis contributes greatly to this field by displaying the development and implementation of different astronomical techniques forRSOs.

5.1.1 Absolute Photometry

The absolute photometry methods discussed in this text describe three different implementations of detection algorithms, each resulting in slight offsets from each other depending on the stars detected in each starfield frame. The results exemplify the importance of consistency in choosing a detection method, utilizing similar filters to those of the catalogue stars used and measuring adequate star-field data for calculating the transformation coefficients. Additional research conducted on this topic was presented in the paper *Preliminary Analysis for Performing Resident Space Object Photometry* written for Canadian Aeronautical and Space Journal (CASJ) and presented at Canadian Aeronautics and Space Institute (CASI) ASTRO 2022.

5.1.2 JWST Tracking and Photometry

Little literature is seen on performing photometry on the space-based sensor JWST, much less so by another space-based sensor. The work performed on this subject matter overcomes the difficulties faced by observing the target and lays the foundation for further studies by defining the necessary steps for tracking and capturing. This research was presented at the Advanced Maui Optical and Space Surveillance Technologies (AMOS) Conference in 2023, along with the associated paper *Image Processing Techniques for Space Situational Awareness – Performing Photometry on James Webb Space Telescope Imagery from NEOSSat*.

5.2 Future Work

5.2.1 Validation

The created software package should be validated by taking images of known star fields and producing transformation coefficients using external software such as MPO Canopus [45].

5.2.2 LEO satellites

The mechanical capabilities of the ground stations used limited the capturing of fast slew-rate RSO such as LEO objects. Similar processing but with modified prediction, tracking and acquisition could be used to perform photometry on the fastest-growing orbital regime in space.

5.2.3 Expanding Airmass Observations

Observations below 30-degree elevations require a much more complex airmass model to calculate the observed objects airmass. As this was outside the scope of the work produced, further work can be done to implement this model. The accuracy of the produced extinction coefficients with an expanded airmass range.

5.2.4 Second-Order Extinction

Second-order extinction coefficients will need to be accounted for in future analysis to produce more accurate results for absolute photometry.

5.2.5 Bessel Filters

Retesting the absolute photometry equation with standard Bessel filters, much more similar to those used in the APASS catalogue, will results in smaller errors caused by using non-standard filters.

5.2.6 Expanding Time Series

The methods and software produced during this thesis should be applied to a wider breadth of data for further research. Although the focus was placed on developing the tools for photometry, applying these tools to create longer time series could provide insights into tumble rates, shape and other photometric parameters. One such example would be to compare calibrated lightcurves of

IntelSat 10-02 to earlier recordings, without the MEV-2 refuelling mission, to determine whether or not features of the docking could be seen. Other studies could be conducted to determine bus types of unknown RSOs to classify them. Additionally expanding the time series of JWST and correlating attitude adjustments will help to further research in RSO reflectance modelling.

5.2.7 Unknown Object Characterization

Expressed in this thesis are processes used for known RSOs, but sometimes it may be required to characterize an unknown object and compare it to a known database. The same methods can be extended to unknown objects to determine their characteristics and potential identify them through the combination of photometric modelling and orbit determination.

Bibliography

[1] *A Practical Guide to Lightcurve Photometry and Analysis*. Springer New York, 2006. DOI: 10.1007/0-387-33391-6. URL: https://doi.org/10.1007%2F0-387-33391-6.

[2] Astropy Collaboration and Astropy Contributors. "Astropy: A community Python package for astronomy". In: 558, A33 (Oct. 2013), A33. DOI: 10.1051/0004-6361/201322068. arXiv: 1307.6212 [astro-ph.IM].

[3] Astropy Collaboration and Astropy Contributors. "The Astropy Project: Building an Open-science Project and Status of the v2.0 Core Package". In: 156.3, 123 (Sept. 2018), p. 123. DOI: 10.3847/1538-3881/aabc4f. arXiv: 1801.02634 [astro-ph.IM].

[4] Astropy Collaboration and Astropy Project Contributors. "The Astropy Project: Sustaining and Growing a Community-oriented Open-source Project and the Latest Major Release (v5.0) of the Core Package". In: *apj* 935.2, 167 (Aug. 2022), p. 167. DOI: 10.3847/1538-4357/ac7c74. arXiv: 2206.14220 [astro-ph.IM].

[5] Roger R. Bate, Donald D. Mueller, and Jerry E. White. *Fundamentals of Astrodynamics*. New York: Dover Publications, 1971.

[6] Donald Bédard and Gregg A. Wade. "Time-resolved visible/near-infrared spectrometric observations of the Galaxy 11 geostationary satellite". In: *Advances in Space Research* 59.1 (2017), pp. 212–229. ISSN: 0273-1177. DOI: https://doi.org/10.1016/j.asr.

2016.08.033. URL: https://www.sciencedirect.com/science/article/pii/S0273117716304860.

[7] Richard Berry and James Burnell. *The handbook of astronomical image processing*. Vol. 2. 2005.

[8] E. Bertin and S. Arnouts. “SExtractor: Software for source extraction.” In: 117 (June 1996), pp. 393–404. DOI: 10.1051/aas:1996164.

[9] M. S. Bessell. “UBVRI passbands.” In: 102 (Oct. 1990), pp. 1181–1199. DOI: 10.1086/132749.

[10] C. Binz et al. “Optical Survey of the Tumble Rates of Retired GEO Satellites”. In: *Advanced Maui Optical and Space Surveillance Technologies Conference*. Ed. by S. Ryan. Sept. 2014, E61, E61.

[11] Larry Bradley et al. *astropy/photutils: 1.9.0*. Version 1.9.0. Aug. 2023. DOI: 10.5281/zenodo.596036.

[12] Frederick R. Chromey. *To Measure the Sky: An Introduction to Observational Astronomy*. Cambridge University Press, 2010.

[13] Matt Craig et al. *astropy/ccdproc: 2.3.1 – fixes astropy 5.1 compatibility*. Zenodo. Version 2.3.1. May 2022. DOI: 10.5281/zenodo.6533213.

[14] Howard D. Curtis. “Chapter 4 - Orbits in Three Dimensions”. In: *Orbital Mechanics for Engineering Students (Second Edition)*. Ed. by Howard D. Curtis. Second Edition. Aerospace Engineering. Boston: Butterworth-Heinemann, 2010, pp. 199–254. ISBN: 978-0-12-374778-5. DOI: https://doi.org/10.1016/B978-0-12-374778-5.00004-0. URL: https://www.sciencedirect.com/science/article/pii/B9780123747785000040.

[15] James Wertz David Vallado. *The Fundamentals of Astrodynamics and Applications,4th Edition*. Microcosm Press, 2013.

[16] Bob Denny. *Pinpoint Astrometric Engine*. URL: http://pinpoint.dc3.com/.

[17] Joshua Fitzmaurice et al. "Detection and correlation of geosynchronous objects in NASA's Wide-field Infrared Survey Explorer images". In: *Acta Astronautica* 183 (2021), pp. 176–198. ISSN: 0094-5765. DOI: https://doi.org/10.1016/j.actaastro.2021.03.009. URL: https://www.sciencedirect.com/science/article/pii/S0094576521001211.

[18] Adam Ginsburg et al. "astroquery: An Astronomical Web-querying Package in Python". In: 157.3, 98 (Mar. 2019), p. 98. DOI: 10.3847/1538-3881/aafc33. arXiv: 1901.04520 [astro-ph.IM].

[19] Jon Giorgini and Don Yeomans. *JPL Horizons API*. Contributors: Alan Chamberlin (web interface, APIs, database); The NAIF group (SPICELIB) (esp. Chuck Acton, Bill Taber, Nat Bachman); Paul Chodas (some subroutines); Major body ephemerides: Ryan S. Park (Planetary ephemerides), Bob Jacobson (Satellites), Marina Brozovic (Satellites). Cognizant Engineering. 2021.

[20] A. A. Henden et al. "VizieR Online Data Catalog: AAVSO Photometric All Sky Survey (APASS) DR9 (Henden+, 2016)". In: *VizieR Online Data Catalog*, II/336 (Jan. 2016), pp. II/336.

[21] Arne A. Henden and Ronald H. Kaitchuck. *Astronomical photometry*. 1982.

[22] W.A. Hiltner. *Astronomical Techniques*. Midway reprints. University Press, 1962. ISBN: 9780226459639. URL: https://books.google.ca/books?id=NRI1AQAAIAAJ.

[23] Steve B. Howell. *Handbook of CCD Astronomy*. 2nd ed. Cambridge Observing Handbooks for Research Astronomers. Cambridge University Press, 2006. DOI: 10.1017/CBO9780511807909.

[24] Alessandro de Iaco Veris. *Practical Astrodynamics*. Springer, 2018.

[25] Dr. T.S. Kelso. *NORAD Two-Line Element Set Format*. URL: https://www.celestrak.com/NORAD/documentation/tle-fmt.php. accessed: 18.11.2021.

[26] Arlo U. Landolt. "UBVRI Photometric Standard Stars in the Magnitude Range 11.5 < V < 16.0 Around the Celestial Equator". In: 104 (July 1992), p. 340. DOI: 10.1086/116242.

[27] Dustin Lang et al. "Astrometry.net: Blind Astrometric Calibration of Arbitrary Astronomical Images". In: 139.5 (May 2010), pp. 1782–1800. DOI: 10.1088/0004-6256/139/5/1782. arXiv: 0910.2233 [astro-ph.IM].

[28] Andy Lawrence et al. "The case for space environmentalism". In: *Nature Astronomy* 6 (Apr. 2022), pp. 428–435. DOI: 10.1038/s41550-022-01655-6. arXiv: 2204.10025 [astro-ph.IM].

[29] Creon Levit and William Marshall. "Improved orbit predictions using two-line elements". In: *Advances in Space Research* 47.7 (Apr. 2011), pp. 1107–1115. DOI: 10.1016/j.asr.2010.10.017. arXiv: 1002.2277 [physics.space-ph].

[30] Lauren Glattly Matt Craig Lauren Chambers. *CCD Data Redcut5ion Guide*. URL: http://www.astropy.org/ccd-reduction-and-photometry-guide/v/dev/notebooks/00-00-Preface.html#.

[31] Jean H. Meeus. *Astronomical Algorithms*. Willmann-Bell, Incorporated, 1991. ISBN: 0943396352.

[32] Brett M. Morris et al. "astroplan: An Open Source Observation Planning Package in Python". In: 155.3, 128 (Mar. 2018), p. 128. DOI: 10.3847/1538-3881/aaa47e. arXiv: 1712.09631 [astro-ph.IM].

[33] Paris Observatory. *Earth Orientation Parameters (EOP) Product Center*. 2021. URL: https://hpiers.obspm.fr/eoppc/eop/eopc04/eopc04.21.

[34] J. Palmer and A. C. Davenhall. "The CCD Photometric Calibration Cookbook". In: *Starlink Cookbook* 6 (Jan. 2001).

[35] W.D. Pence et al. “Defintion of the Flexible image Transport System (FITS) version 3.0”. In: Astronomy and Astrophysics (Dec. 2010), pp. 1–40. DOI: https://doi.org/10.1051/0004-6361/201015362.

[36] Brandon Rhodes. *Skyfield: High precision research-grade positions for planets and Earth satellites generator*. Astrophysics Source Code Library, record ascl:1907.024. July 2019. ascl: 1907.024.

[37] R. Scott, K. Bernard, and S. Thorsteinson. “Combined Space-Based Observations of Geostationary Satellites”. In: *Advanced Maui Optical and Space Surveillance Technologies Conference*. Ed. by Sandy Ryan. Sept. 2016, 20, p. 20.

[38] R. Scott and B. Wallace. “Satellite characterization using small aperture instruments at DRDC Ottawa”. In: *Advanced Maui Optical and Space Surveillance Technologies Conference*. Ed. by C. Paxson et al. Jan. 2008, E36, E36.

[39] D. L. Shupe et al. “The SIP Convention for Representing Distortion in FITS Image Headers”. In: *Astronomical Data Analysis Software and Systems XIV*. Ed. by P. Shopbell, M. Britton, and R. Ebert. Vol. 347. Astronomical Society of the Pacific Conference Series. Dec. 2005, p. 491.

[40] D. L. Shupe et al. “The SIP Convention for Representing Distortion in FITS Image Headers”. In: *Astronomical Data Analysis Software and Systems XIV*. Ed. by P. Shopbell, M. Britton, and R. Ebert. Vol. 347. Astronomical Society of the Pacific Conference Series. Dec. 2005, p. 491.

[41] S. Thorsteinson. “Key Findings from the NEOSSat Space-Based SSA Microsatellite Mission”. In: 2018. URL: https://api.semanticscholar.org/CorpusID:201035349.

[42] Doug Tody. “IRAF in the Nineties”. In: *Astronomical Data Analysis Software and Systems II*. Ed. by R. J. Hanisch, R. J. V. Brissenden, and J. Barnes. Vol. 52. Astronomical Society of the Pacific Conference Series. Jan. 1993, p. 173.

[43] Doug Tody. “The IRAF Data Reduction and Analysis System”. In: *Instrumentation in astronomy VI*. Ed. by David L. Crawford. Vol. 627. Society of Photo-Optical Instrumentation Engineers (SPIE) Conference Series. Jan. 1986, p. 733. DOI: 10.1117/12.968154.

[44] David A. Vallado and Wayne D. McClain. *Fundamentals of Astrodynamics and Applications*. 3rd. New York: Springer, 2007.

[45] Brian D. Warner. *MPO Software: An OVernight Success*. 2014.

[46] Donald G. York et al. “The Sloan Digital Sky Survey: Technical Summary”. In: 120.3 (Sept. 2000), pp. 1579–1587. DOI: 10.1086/301513. arXiv: astro-ph/0006396 [astro-ph].

[47] N. Zacharias et al. “THE FOURTH US NAVAL OBSERVATORY CCD ASTROGRAPH CATALOG (UCAC4)”. In: *The Astronomical Journal* 145.2 (Jan. 2013), p. 44. DOI: 10.1088/0004-6256/145/2/44. URL: https://doi.org/10.1088%2F0004-6256%2F145%2F2%2F44.

[48] N. Zacharias et al. “The Fourth US Naval Observatory CCD Astrograph Catalog (UCAC4)”. In: 145.2, 44 (Feb. 2013), p. 44. DOI: 10.1088/0004-6256/145/2/44. arXiv: 1212.6182 [astro-ph.IM].

[49] Xiao-Fen Zhao et al. “Multicolor photometry of geosynchronous satellites and application on feature recognition”. In: *Advances in Space Research* 58.11 (2016), pp. 2269–2279. ISSN: 0273-1177. DOI: https://doi.org/10.1016/j.asr.2016.09.020. URL: https://www.sciencedirect.com/science/article/pii/S0273117716305336.